Journal of Fluids and Structures (1997) **11,** 33–72

COMPUTER-AIDED FLOW VISUALIZATION AND VORTICITY BALANCE IN THE LAMINAR WAKE OF A CIRCULAR CYLINDER

P. ANAGNOSTOPOULOS
Department of Civil Engineering, University of Thessaloniki
Thessaloniki 54006, Greece

(Received 12 April 1995 and in revised form 22 July 1996)

The two-dimensional Navier-Stokes equations were used for the solution of laminar vortex shedding behind a circular cylinder at a Reynolds number of 106 using the finite element technique. Streamlines, equivorticity lines and filament lines have been used for the wake visualization, while the pressure distribution in the wake is presented in the form of isobars. Useful conclusions have been drawn from the superposition of different flow visualization patterns, a technique used extensively herein. The strengths of the laminar vortices were calculated at various locations from the vorticity distribution, confirming the hypothesis that maximum strength occurs at the end of the formation region. A vorticity balance in the cylinder wake was conducted, comparing the circulation influx into the wake over a period and the strength of the vortices. The time-dependent streamwise fluid velocities were calculated from the present simulation at various points in the wake, and are presented on the same diagram with velocities measured experimentally at similar conditions. The validity of alternative definitions for the vortex formation length was examined and the velocity and displacement of the newly formed vortex as function of time was calculated.

1. INTRODUCTION

VORTEX SHEDDING BEHIND A CIRCULAR CYLINDER is a complicated flow phenomenon which has proved a challenging area for researchers over a long number of years. In the fifteenth century Leonardo da Vinci sketched a double row of vortices in the wake of a bluff body. Strouhal (1878) demonstrated that the dimensionless frequency, fd/U, remains constant over a wide range of Reynolds numbers, while von Kármán (1911) replaced the actual vortex street with a double row of point vortices and proposed a stability criterion for its existence. Various investigators continued the research on vortex shedding behind a bluff body, and many of them focused their attention on low Reynolds numbers, where the phenomenon is less complicated due to the absence of turbulence. Moreover, the increase of power of digital computers made possible the numerical solution of the phenomenon, from the integration of the Navier-Stokes equations.

Tritton (1959) investigated experimentally the phenomenon of laminar vortex shedding in water, and reported a transition in the mechanism of vortex shedding at $\mathrm{Re} = 100$ which became a strong source of debate. Zdravkovich (1969) performed flow visualization experiments in air and reported the absence of dye in the cores of the vortices at the side of the cylinder where the dye had been injected. Gerrard (1978) conducted a detailed flow visualization study of vortex street wakes at low Reynolds numbers and found a discontinuity in the time taken for a vortex to accelerate to its final convective velocity at $\mathrm{Re} = 100$, and, most importantly, indicated a strong

0889–9746/97/010033 + 40 $25.00/fl960066

transition in the strength of the shed vortex at this Reynolds number. Perry *et al.* (1982) examined experimentally the instantaneous streamline and streakline patterns of the vortex street wake behind a circular cylinder and introduced critical points, where the slopes of the streamlines become indeterminate. Flow visualization experiments conducted by Tritton (1959), Gerrard (1978) and Williamson (1989) reveal that even at very low Reynolds numbers the vortex lines have a bowed appearance and the vortices are shed from the cylinder at a slanted angle. Karniadakis & Triantafyllou (1989) found numerically a continuous variation of the Strouhal number with the Reynolds number at Re between 50 and 240 which led to the conclusion that discontinuities in the two-dimensional flow as found by Tritton seem unlikely. Green & Gerrard (1991) used an optical interferometer for the visualization of the wake behind a circular cylinder moving in a water tank. From the very small deformation of the free surface they calculated the strength and age of the vortices as functions of the distance from the cylinder. More recently (1993) the same researchers measured the vorticity and shear stress distributions behind a circular cylinder at Reynolds numbers between 73 and 226, and they used the vorticity distribution for the determination of the vortex strength in the near wake. In addition, they proposed a vortex-shedding mechanism at low Reynolds numbers, different from that suggested by Gerrard (1966) at higher Reynolds numbers.

With the advent of digital computers, various computational solutions of the phenomenon have been presented in the ''stable range'', where the vortex street wake is laminar. Most of them are based on the two-dimensional Navier–Stokes equations and they employ finite difference or finite element schemes. Jordan & Fromm (1972), Swanson & Spaulding (1978) and Franke *et al.* (1990) used the finite difference method for the numerical solution of unsteady flow around a circular cylinder, while Smith & Brebbia (1977), Gresho *et al.* (1980), Eaton (1987), Karniadakis & Triantafyllou (1989) and Anagnostopoulos (1989) favoured the finite element technique. The numerical solutions provide a good description of the flow parameters throughout the solution domain, a task which is difficult to be accomplished experimentally, especially in unsteady flows. However, their accuracy depends on various factors such as the method of solution, the mesh refinement and the boundary conditions. A point of interest is that the computed stream function diagrams are in disagreement with the experimental observations by Perry *et al.* (1982). The experimental observation by Perry *et al.* suggests that the so called ''centres'' and ''saddles'' of two shed vortices coexist, while the streamline patterns obtained numerically show the centre and saddle of a shedding vortex disappearing before a new vortex is shed. Moreover, since the flow pattern behind a circular cylinder exhibits three-dimensional chracteristics even at very low Reynolds numbers [just over 64 according to Williamson (1989)], the validity of two-dimensional numerical models has been questioned.

In the present study, although the streamlines and the filament lines were used extensively for the interpretation of flow phenomena associated with vortex shedding, great importance was given to the equivorticity lines. The reason for favouring the equivorticity lines is twofold; the instantaneous centres of the vortices are the points where the absolute values of vorticity becomes maximum, and the strength of the vortices can be calculated from the vorticity distribution. Moreover, the pressure distribution in the wake is presented in the form of isobars. For better interpretation of the information carried by different flow parameters and for the determination of the relevance between the characteristic lines which describe a flow field, the contours of two different field variables at the same time instant were plotted on the same graph. The time history of fluid velocities in the streamwise direction is depicted at some

points in the wake, while mean velocities and r.m.s. values of velocity fluctuation over a shedding cycle are also presented.

2. THE NUMERICAL SOLUTION

2.1. The Computational Method

The two-dimensional Navier-Stokes equations were transformed, by eliminating the pressure, into a pair of equations containing the stream function, Ψ, and the vorticity, ζ, as field variables. For the calculation of pressure throughout the flow field a third equation of the Poisson type is available. The present formulation of the Navier-Stokes equations was favoured over the formulation in terms of primitive variables, because the streamlines and the equivorticity lines can be obtained directly from the nodal values of Ψ and ζ, and simple three-node triangular elements can be used, since continuity only of the field variables at the element interfaces is required (C^0 continuity). The numerical solution of the problem was performed at $\mathrm{Re} = 106$ using the Galerkin finite element method. The nodal values of Ψ and ζ were calculated at each time step and the two components of the fluid velocity (u and v) were determined from the values of Ψ at the nodal points of the solution domain. Having calculated the values of u and v throughout the flow domain Poisson's equation was solved to yield the nodal values of pressure. The main features of the procedure followed herein have been described in detail by Anagnostopoulos (1989).

2.2. The Computational Mesh and Blockage Effects

The finite element mesh used for the solution is depicted in Figure 1. It contains 5 801 nodes and 11 244 three-node triangular elements. The solution domain extends five cylinder diameters upstream from the cylinder, 10 diameters above and below the cylinder and 22 diameters downstream from the cylinder. The refinement of the mesh was increased behind the cylinder where the vortices are formed and reduced far from the cylinder in the cross-flow direction for reasons of economy. The solution domain was extended considerably above and below the cylinder in order to reduce the numerical blockage effect and obtain a numerical solution approximating as much as possible flow conditions in an unbounded flow field. As reported by Chilukuri (1987), Karniadakis & Triantafyllou (1989) and Anagnostopoulos (1994), the truncation of the solution domain in the cross-flow direction has as effect the increase of the effective approaching velocity. For correction of blockage effects Allen & Vincenti (1944) have proposed the formula quoted by Roshko (1961),

$$\frac{U}{U'} = 1 + \tfrac{1}{4} C_D' \left(\frac{d}{h}\right) + 0{\cdot}82 \left(\frac{d}{h}\right)^2, \tag{1}$$

where U and U' are the corrected and real values of the approaching stream velocity, C_D' is the drag coefficient without the blockage correction, and h the width of the passage. The validity of formula (1) to Reynolds number in the stable range has been confirmed by Anagnostopoulos (1994). From previous solutions in the area of Reynolds number considered, C_D' was found to be approximately equal to 1·30; therefore, for $d/h = 0{\cdot}05$, equation (1) yields $U/U' = 1{\cdot}018$ and the effect of blockage on the freestream velocity is small. The cylinder diameter was set at 1·6 mm, equal to that used in the experiment, the freestream velocity was 0·066 m/s, and the fluid used

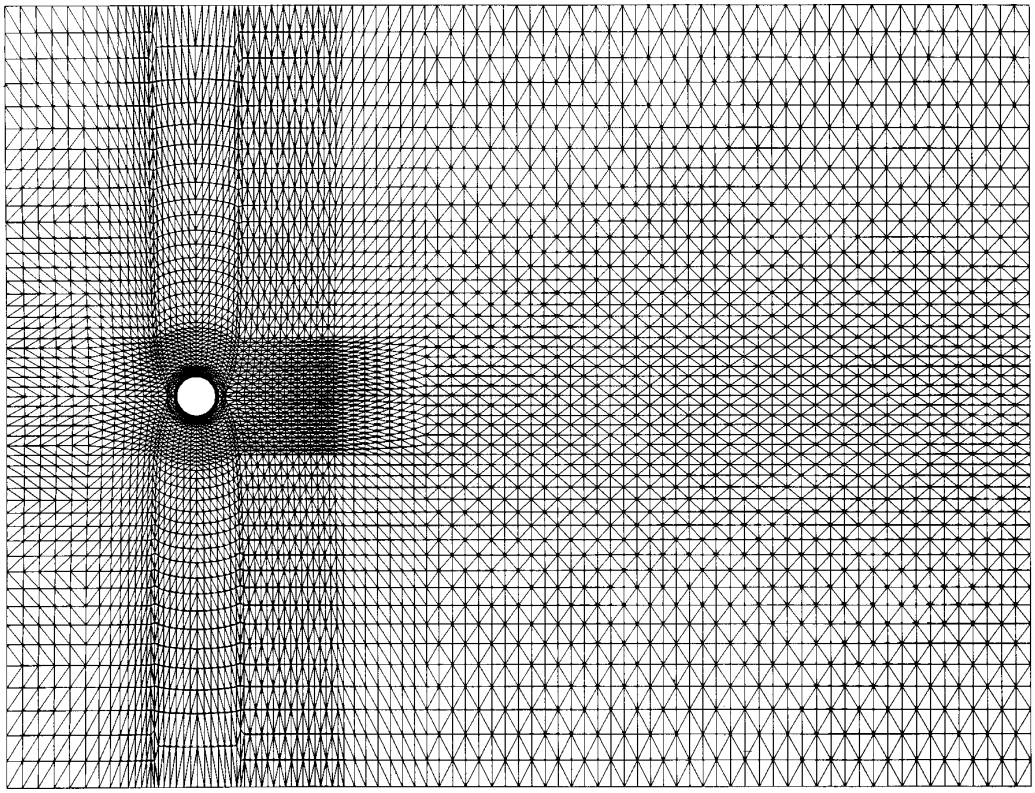

Figure 1. The finite element mesh.

was water with kinematic viscosity $\nu = 10^{-6}\,\mathrm{m}^2/\mathrm{s}$, yielding a Reynolds number equal to 106.

2.3. Boundary Conditions and Solution Procedure

The vorticity throughout the inflow and the upper and lower boundaries was set equal to zero. At the outflow boundary the boundary condition was approximated by the formula $\partial\zeta/\partial n = 0$. At the point W on the cylinder surface the vorticity was calculated from

$$\zeta_W = \frac{\Psi_W - \Psi_I}{\Delta n^2} - \frac{\zeta_I}{2}, \tag{2}$$

where I is a point of the flow field lying on the normal to the cylinder through W, at a distance Δn from point W.

The values of the stream function at the inflow boundary vary linearly from $-\frac{1}{2}Uh$ at the lowermost point to $\frac{1}{2}Uh$ at the uppermost. The upper and lower boundaries are streamlines, therefore the value of Ψ was set equal to $\frac{1}{2}Uh$ along the upper boundary and $-\frac{1}{2}Uh$ along the lower boundary. The value of Ψ on the cylinder surface can be evaluated from the continuity of pressure along the cylinder boundary. Along the solid boundary the equation of motion due to the no-slip condition takes the form

$$\frac{\partial p}{\partial s} = -\rho\nu\frac{\partial\zeta}{\partial n}, \tag{3}$$

where s is the direction along and n normal to the boundary. The continuity of pressure along the cylinder surface expressed in mathematical terms dictates that

$$\oint \frac{\partial \zeta}{\partial n} \mathrm{d}s = 0. \tag{4}$$

If W denotes a point on the solid boundary and I a point on the normal to the boundary through W at a distance Δn, equation (4) can be written as

$$\oint \frac{\zeta_I - \zeta_W}{\Delta n} \mathrm{d}s = 0. \tag{5}$$

Substitution of ζ_W from equation (2) in equation (5) after some manipulation yields

$$\oint [\Delta n^2 \zeta_I + 2(\Psi_I - \Psi_W)] \, \mathrm{d}s = 0. \tag{6}$$

Consequently, if the values of Ψ_I and ζ_I have been calculated at a time step, the value of the stream function on the cylinder surface Ψ_W can be derived from integral (6), to be used as boundary condition at the following time step. At the outflow boundary, the boundary condition used was $\partial \Psi / \partial n = 0$, where n is the direction normal to the boundary. This boundary condition is not absolutely correct, but, since the boundary is far downstream from the cylinder, it does not seem to influence the phenomena near the cylinder.

The pressure throughout the flow field was determined from the solution of Poisson's equation. The boundary conditions for pressure at the outer boundaries are the same as for the vorticity. On the cylinder surface the boundary condition $\partial p / \partial n$ was derived as follows. The equation of motion along the radial direction on the cylinder surface due to the no-slip condition is simplified to

$$-\frac{1}{\rho}\frac{\partial p}{\partial n} + \nu\left(\frac{\partial^2 v_r}{\partial^2 s} + \frac{\partial^2 v_r}{\partial^2 n}\right) = 0, \tag{7}$$

where v_r is the component of the fluid velocity in the radial direction, s is the tangential direction on the cylinder surface and n is the outward normal. The derivative of vorticity,

$$\frac{\partial \zeta}{\partial s} = \frac{\partial^2 v_r}{\partial^2 s} - \frac{\partial^2 v_s}{\partial s \, \partial n},$$

from the continuity equation $\partial v_s / \partial s + \partial v_r / \partial n = 0$ becomes

$$\frac{\partial \zeta}{\partial s} = \frac{\partial^2 v_r}{\partial^2 s} + \frac{\partial^2 v_r}{\partial^2 n}. \tag{8}$$

From equations (7) and (8) the boundary condition $\partial p / \partial n$ was derived as

$$\frac{\partial p}{\partial n} = \mu \frac{\partial \zeta}{\partial s}. \tag{9}$$

The initial values of the vorticity throughout the flow field were set equal to zero. At each time step the nodal values of the stream function, vorticity and pressure were calculated. As the computation proceeded, a pair of symmetric vortices started to form behind the cylinder, continually growing in size under the action of viscosity. When the size of the standing vortices was almost stabilized, very small asymmetries were detectable in the wake caused by round-off errors, which increased eventually with

time. The shedding process may be accelerated by introducing at a time step a small disturbance in the flow, usually accomplished by adding a small amount of vorticity at a nodal point on the wake axis. The computation continued until the wake became fully periodic, displaying the characteristics of a completely established vortex street.

3. DESCRIPTION OF THE FLOW FIELD

The description of the flow field is performed by plotting the streamlines, the equivorticity lines and the filament lines or streaklines. In addition, the isobars, which are defined as the lines of equal pressure, illustrate the pressure distribution throughout the flow field. The streamlines, equivorticity lines and isobars can be generated at each time step from the nodal values of the stream function, vorticity and pressure obtained from the numerical solution. The filament lines are defined as the locus of positions of massless particles which have emerged at a specified point in the flow field.

The vorticity throughout the domain has been nondimensionalized from the formula $\zeta^* = \zeta\, \mathrm{d}/2U$. The numbers of the vorticity contours are displayed in Figure 5 (to be discussed later), and the associated dimensionless vorticity values are given in Table 1.

The pressures derived numerically have been rendered nondimensional from the formula $p^* = p/\frac{1}{2}\rho U^2$. The numbers of the pressure contours corresponding to the dimensionless pressure values of Table 2 are presented later in Figure 24.

4. VORTICITY DISTRIBUTION IN THE LAMINAR WAKE

The determination of the vorticity distribution in the vortex street wake is of primary importance for the following reasons. The centres of the vortices are the points where the absolute values of vorticity becomes maximum, therefore the equivorticity lines provide a powerful tool for the determination of the vortex street geometry. In addition, the strengths of the vortices can be calculated, and if multiplied by the shedding frequency the rate at which circulation is carried by the wake can be determined.

TABLE 1
Vorticity contour values

Contour number	ζ^*	Contour number	ζ^*
1	−5·0	−1	5·0
2	−3·0	−2	3·0
3	−2·0	−3	2·0
4	−1·75	−4	1·75
5	−1·40	−5	1·40
6	−1·30	−6	1·30
7	−1·20	−7	1·20
8	−1·10	−8	1·10
9	−1·0	−9	1·0
10	−0·8	−10	0·8
11	−0·6	−11	0·6
12	−0·4	−12	0·4
13	−0·2	−13	0·2
14	−0·1	−14	0·1
15	−0·05	−15	0·05
16	−0·02	−16	0·02

TABLE 2
Values of pressure contours

Contour number	p^*	Contour number	p^*	Contour number	p^*
1	0·80	−1	−1·0	1′	0·070
2	0·70	−2	−0·9	2′	0·065
3	0·60	−3	−0·8	3′	0·060
4	0·50	−4	−0·7	4′	0·055
5	0·40	−5	−0·6	5′	0·050
6	0·30	−6	−0·5	6′	0·045
7	0·20	−7	−0·4	7′	0·040
8	0·10	−8	−0·35	8′	0·035
9	0·095	−9	−0·30	9′	0·030
10	0·090	−10	−0·25	10′	0·025
		−11	−0·20	11′	0·020
		−12	−0·15	12′	0·015
		−13	−0·10	13′	0·010
		−14	−0·05	14′	0·005

4.1. THE EQUIVORTICITY LINES THROUGHOUT THE SOLUTION DOMAIN

The equivorticity lines throughout the solution domain at $t/T = 0$ are depicted in Figure 2. As origin of time was taken the instant at which the fluctuating lift force on the cylinder becomes zero, turning from positive to negative. Eight vortices are shown, four on each side of the wake axis. The minimum absolute vorticity contour with end points on the cylinder encompasses vortices I and III, rendering the exact determination of the vortex boundaries difficult. Vortex IV which is still surrounded, together with vortex II, by the outermost vorticity contour, is about to be detached. When all the equivorticity contours of a vortex have just been detached to form closed loops, the vortex appears in elongated form, with the longer axis almost perpendicular to the wake centreline. Then, it acquires a rounder shape as it moves downstream, more similar to that of an Oseen vortex. Another interesting feature is the low absolute vorticity contours drawn towards the adjacent vortex of opposite sign in the downstream direction, which has as effect the cancellation of vorticity at the vortex boundaries. This is the situation occurring between the pairs of vortices IV–V, V–VI and VI–VII. The vorticity cancellation phenomenon is interpreted from the reduction of size of the ''tail'' formed by the vorticity contour closest to the outermost, in the

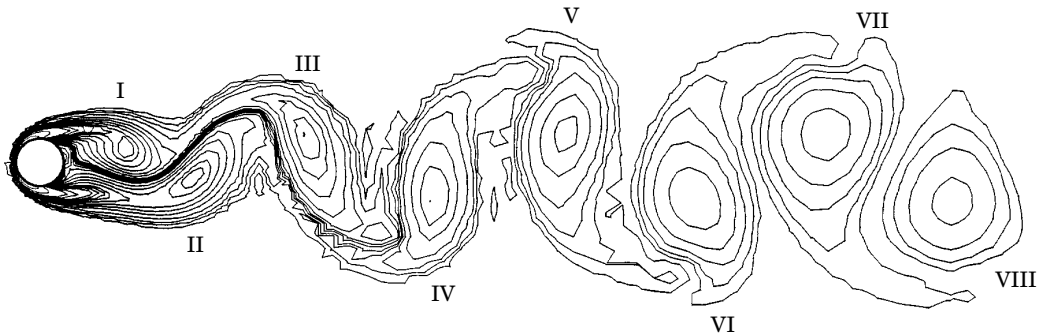

Figure 2. Equivorticity lines throughout the solution domain at $t = 0$.

sequence of vortices IV to VI; although in vortex IV it almost extends to the vortex boundary, in vortex VI it has disappeared. The measurement of vorticity in the wake of a cylinder is a formidable task, and the relevant investigations known to the author are those by Green (1989) and by Okude & Matsui (1990). Green confined his measurements to a small part of the wake near the cylinder at Reynolds numbers between 73 and 226 while Okude & Matsui performed a detailed vorticity measurement at a great distance behind the cylinder at $\mathrm{Re} = 140$. Green's vorticity distribution at $\mathrm{Re} = 100$ agrees in general terms with the results of the present solution at equivalent time steps, although differences are present in some cases. On the other hand, the equivorticity contours presented by Okude and Matsui are in close agreement with those of the present computation. This detailed investigation confirmed the numerical result found herein, according to which the outer vorticity contour of a vortex is drawn close to the downstream vortex of opposite vorticity, causing a local distortion of the equivorticity lines and leading to vorticity cancellation.

4.2. Superposition of Streamline Pattern on the Equivorticity Lines

The streamlines over one half of a shedding cycle were superimposed on the equivorticity lines in Figure 3. It can be clearly seen that, near the cylinder, the centres of the vortices do not coincide with the rotating masses of fluid interpreted in the form of closed streamlines, which are surrounded by instantaneous alleyways. As the vortices are convected downstream the closed streamline region decreases in size, whereas the number of alleyways increases. In frame 3(c) closed streamline loops of the shedding vortex are not detectable any more. Figure 3 also provides a good interpretation of the "vortex splitting" process detected by Green & Gerrard (1993). In Figure 3 (a) the separating streamline emerging from the upper part of the cylinder divides the fluid entering into the wake above the cylinder from that drawn from the lower part by the alleyways. The alleyways transfer positive vorticity fluid from the lower part of the cylinder across the wake, causing reduction of the value of the negative vorticity prevailing locally. This reduction of vorticity is manifested as the local distortion of the vorticity contours, which seem to approach their opposite part farthest from the cylinder in the form of a neck. Eventually the two opposite parts of the equivorticity line come into contact and the contour is split in two parts: a closed loop associated with the shedding vortex and a line starting and ending on the cylinder.

4.3. Vortex Strength and Vorticity Balance

The description by von Kármán of the periodic wake behind a bluff body in terms of point vortices is well known. Various researchers (Hooker 1936; Schaefer & Eskinazi 1958; Griffin & Ramberg 1974) improved this model by considering viscous effects. The ideal vortices introduced by von Kármán were replaced by Oseen vortices throughout the flow field or in the neighbourhood of the points under consideration. The characteristic parameters of the vortex street such as the strength and spacing of the vortices are obtained by matching measured velocity profiles with the appropriate models. Although the results of these models are considered as reliable in general terms, the models are based on assumptions, the most important of which is that the vortices diffuse as they are convected downstream as if they were isolated. The strengths of the vortices are considered constant, while in reality there is a reduction of vortex strength with downstream distance resulting from the mutual cancellation of opposite-sign vorticity. The vortex strength obtained from each model is multiplied by

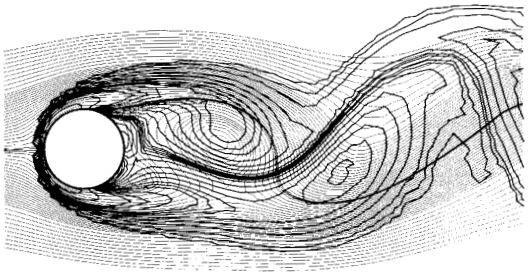

(a) $t/T = 0$

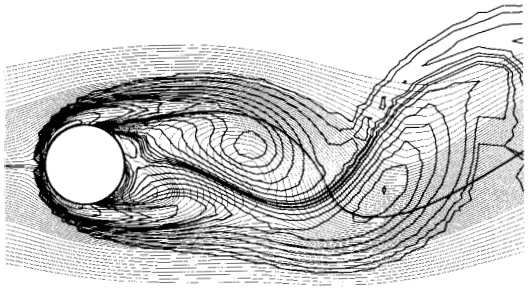

(b) $t/T = 1/8$

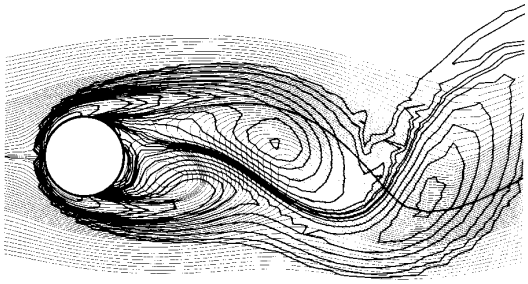

(c) $t/T = 2/8$

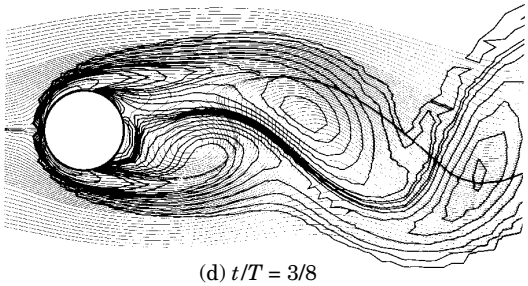

(d) $t/T = 3/8$

Figure 3. Equivorticity lines superimposed on the streamline pattern in the near wake separated by a time interval of $T/8$.

the shedding frequency to determine the rate at which vorticity is carried away by the wake. The rate of vorticity generation by the cylinder is determined by boundary layer principles in conjunction with velocity or base-pressure measurements. The difference between the vorticity generated and that contained in the vortices is assumed to have been cancelled by vorticity of the opposite sign. Birkhoff & Zarantonello (1957) expressed the rate of vorticity contained in the vortices as

$$K = \Gamma f = \Lambda U^2, \tag{10}$$

where Γ is the circulation of a vortex, f the shedding frequency and Λ a dimensionless parameter. Berger (1964) found $\Lambda = 0{\cdot}395$ at $\mathrm{Re} = 65$ and $\mathrm{Re} = 151$, while Griffin & Ramberg (1974) report $\Lambda = 0{\cdot}45$ for $\mathrm{Re} = 144$. Berger & Wille (1972) quote the ratio of the vorticity lost by cancellation to the vorticity generated by the cylinder over a wide range of Reynolds numbers, as found by various investigators. For Reynolds numbers in the stable range, the reported vorticity surviving in the vortices is 40% of the vorticity generated by the cylinder.

Okude & Matsui (1990) from their vorticity measurements calculated the vortex strength from the well-known relationship between circulation and vorticity. The measurements of Okude & Matsui (1990) confirm the continuous decrease of vortex strength with downstream distance from the cylinder. Green & Gerrard (1991) conducted an optical interferometric study for the visualization of the wake behind a circular cylinder at low Reynolds numbers. They used an optical interferometer in order to measure the very small free surface displacements in the wake of a cylinder moving in a towing tank and they derived the strength and age of the vortices from the free surface profiles. They confirmed the existence of a peak in vortex strength at $\mathrm{Re} = 100$ which had been found previously by superposition of data from different studies, and they presented the proportion of loss of circulation for Reynolds numbers between 70 and 120. The vorticity surviving at Re around 100 was found to be 68% of the vorticity shed, much higher than the value 40% quoted by Berger & Wille (1972).

Apart from the experimental results mentioned previously, Eaton (1987) performed a vorticity balance in the wake of a cylinder computationally. He considered a line segment perpendicular to the freestream, extending from the separation point A to the outer boundary B and calculated the amount of vorticity passing through the segment AB over a shedding period T from the integral

$$\int_0^T \int_A^B u\zeta \, \mathrm{d}y \, \mathrm{d}t. \tag{11}$$

Then he considered the distortion of the ''material element'' AB over one and two shedding periods and evaluated the surviving vorticity within the areas formed from the contour integral of the circulation (Stokes' theorem). The results of the vorticity balance show that only 11% of the vorticity shed in one period is cancelled during one period and 40% during two periods.

The vorticity balance conducted by Eaton estimates the cancellation of vorticity in the same bulk of fluid as it deforms moving downstream. The calculation of the strength of the vortices as they are convected downstream and the ratio of the vorticity lost by cancellation will be described in what follows. For the calculation of the amount of the vorticity carried into the wake over a shedding period, equation (11) was also used. The separation point A, whose location on the cylinder was fluctuating, was determined at each time step. Then the line AB parallel to the inflow boundary was drawn from point A to the outer boundary, as shown in Figure 4. The values of the vorticity ζ and the streamwise velocity u at the intersection of line AB with the

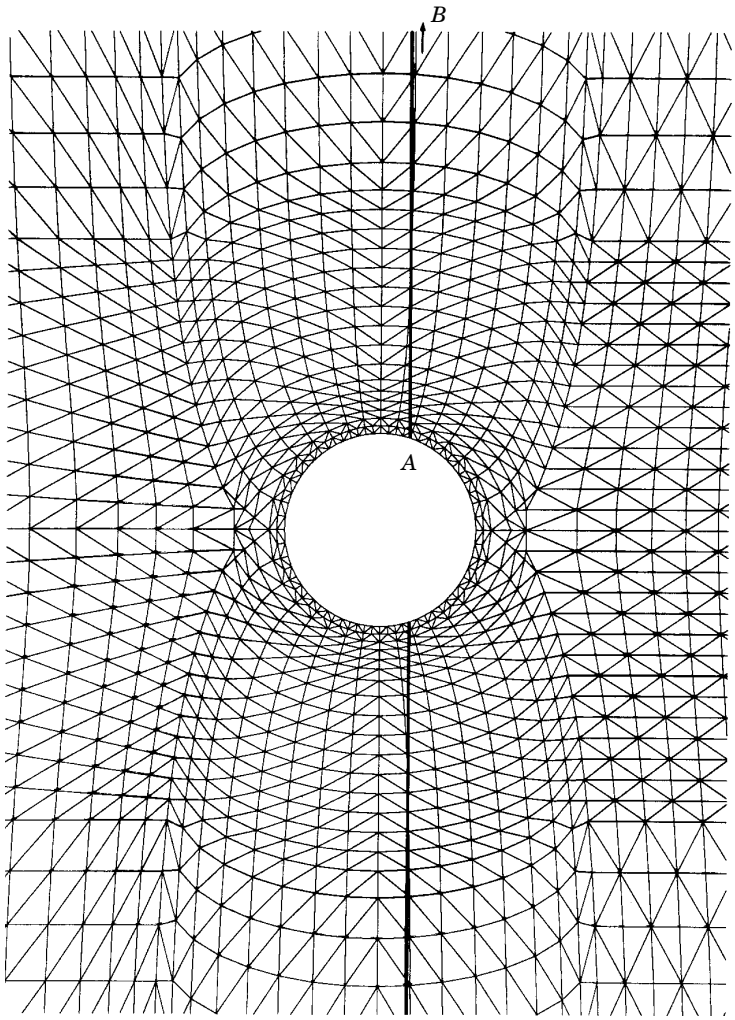

Figure 4. Definition sketch. A denotes the separation point, and B lies on the upper boundary.

element boundaries were calculated from their nodal values using linear interpolation. The vorticity shed from one side of the cylinder during one period normalized by Ud was found equal to 5·29.

The circulation of each vortex was calculated from the equivorticity lines throughout the solution domain, as they are displayed in Figure 2. The technique is based on the Stokes' theorem between the vorticity and the circulation, namely

$$\Gamma = \iint \zeta \, \mathrm{d}s,$$

where s denotes the area around which the circulation is determined. For the evalution of the circulation of each vortex the area enclosed by two consecutive equivorticity lines was calculated, and multiplied by the average of vorticity on these lines. The total circulation of each vortex was calculated from the summation of partial circulations between neighbouring equivorticity contours. The procedure is straightforward at some distance behind the cylinder where all equivorticity contours of each vortex form

closed loops. For the vortices close to the cylinder, as boundary was regarded as the position where the equivorticity line with end points on the cylinder bounding the outermost closed vorticity loop becomes narrowest, as shown in Figure 5. This is the location of local maximum pressure, as will be explained later. In Figure 5 the boundaries between vortices are marked with dashed lines. Although the upstream boundaries of the vortices farthest from the cylinder can be considered as well defined, there exists some arbitrariness in the definition of the upstream boundary of the vortex closest to the cylinder. The calculation of the vortex strength was preformed for the first time when its centre was located 1·5 diameters downstream from the cylinder centre. Then the equivorticity lines were generated at successive short time intervals and the circulation of the vortex as it grows was calculated as described. The vortex strength Γ, normalized by πUd, as a function of the distance from the cylinder is depicted in Figure 6. The vortex strength increases abruptly as the vortex grows, acquiring its maximum value equal to 1·23 at $x/d = 3{\cdot}05$, and afterwards starts to decrease gradually. Therefore, at a specified Reynolds number, only the maximum strength value is unique, and when the strength of a vortex is quoted the location of its centre should also be indicated. Figure 6 reveals that when x/d lies between 8·5 and 14, the vortex strength remains almost constant; the average value of $\Gamma/\pi Ud$ within this interval is 1·08 and its reduction is less than 2%. Figure 2 illustrates that the centre of vortex IV is located approximately at $x/d = 8{\cdot}5$, whereas the displacement of vortex VI divided by the diameter is very close to 14. Consequently, when a vortex is displaced from the position IV of Figure 2 to VI of the same figure, diffusion of vorticity is prominent, while the amount of cancellation is small. Green & Gerrard (1991) also report that the cancellation of vorticity in the range $8 < x/d < 13{\cdot}5$ is very small, a result which is in very good agreement with the present investigation, although it was derived from a different principle.

Another matter of interest is the ratio of the vorticity loss by cancellation to the vorticity generated by the cylinder. The exact rate of circulation carried in the wake K_s can be calculated only from a numerical solution. Otherwise, it can be derived from the formula $K_s = 0{\cdot}5U_s^2$, where U_s is the mean velocity at the edge of the boundary layer at separation. From the Bernoulli equation, $U_s = U(1 - C_{pb})^{1/2}$, where C_{pb} is the base pressure coefficient. For $U = 0{\cdot}066$ and $C_{pb} = -0{\cdot}7$, which are the values of the present computation, K_s was calculated equal to $3{\cdot}72 \times 10^{-3}$, therefore the vorticity shed in the wake over a period equal to 0·146 s is $5{\cdot}44 \times 10^{-4}$, which, if divided by Ud, yields 5·16. The exact value of the vorticity influx found from integral (11) was 5·29, the difference between the two values being only 2·5%. Consequently, provided that a correct value for C_{pb} is used, the approximate technique for the determination of K_s is accurate enough and can be used for the evaluation of vorticity influx. The vorticity surviving when the vortex strength has reached the maximum value is 73%, while it is equal to 65% at $x/d = 13{\cdot}5$. The value reported by Green & Gerrard (1991) at Re = 100 is 68%, very close to the average of these two values.

5. THE STREAKLINES

The simplest and most popular technique of flow visualization is the tracing of the motion of fluid particles. If dye is injected at a fixed point in the flow field, the locus of the fluid particles that passed from that point and thus have been coloured yield the filament lines or streaklines. Various investigators conducted flow visualization experiments of vortex streets by generating streaklines. Taneda [quoted by Van Dyke (1982)], Perry *et al.* (1982) and Gerrard (1978) generated streaklines in water, while

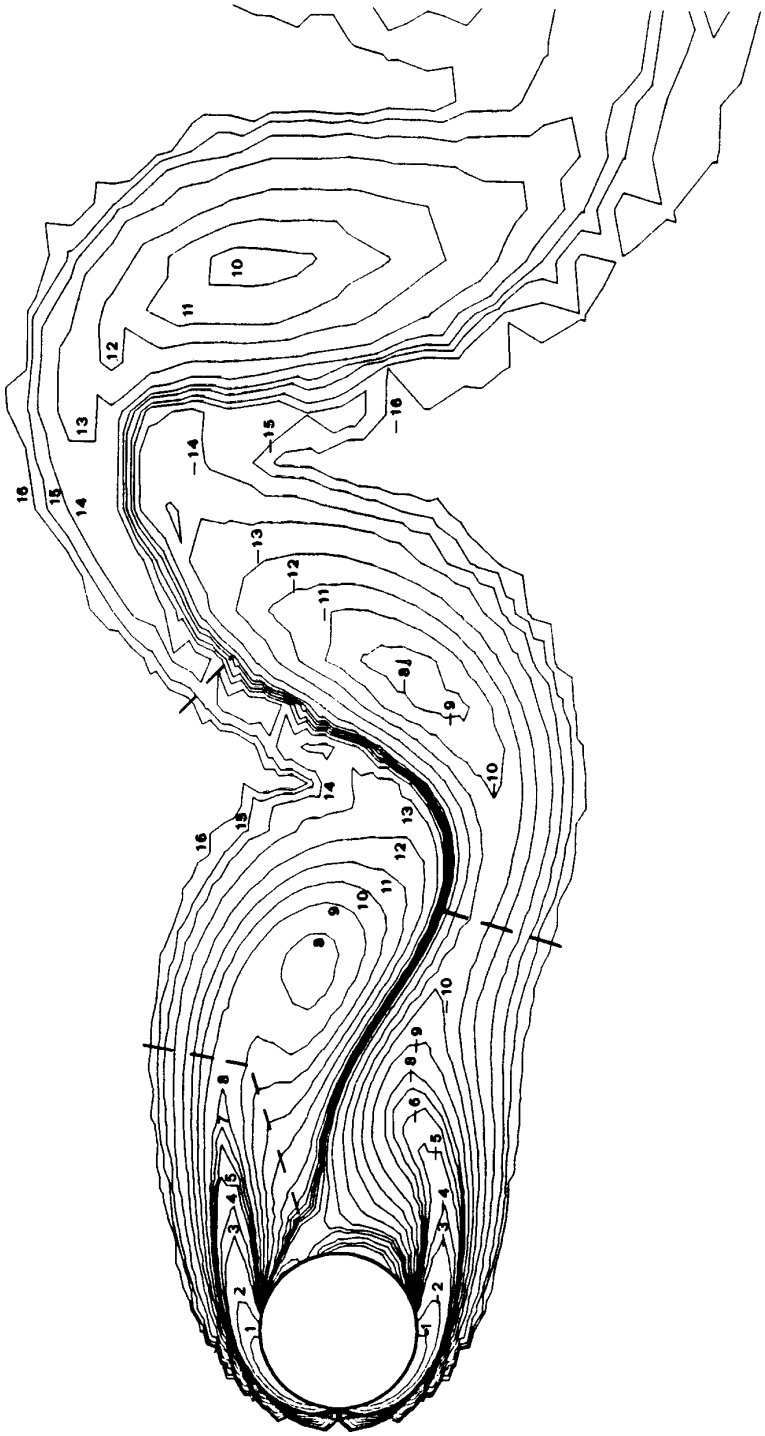

Figure 5. Definition of vortex boundaries for the determination of vortex strength, and vorticity contour numbers.

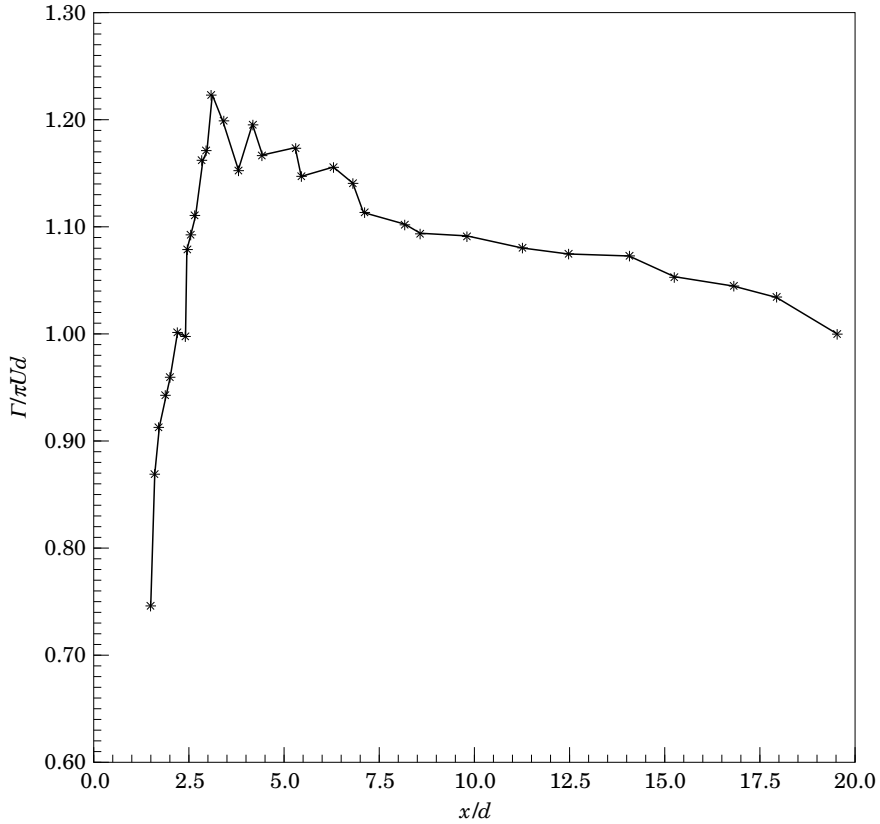

Figure 6. Vortex strength as function of downstream distance from the cylinder.

Koopmann (1967), Zdravkovich (1969), Griffin & Ramberg (1974) and Freymuth *et al.* (1986) used smoke for the visualization of vortex streets in air.

5.1. Streakline Pattern Throughout the Domain

The graphical representation of the streaklines obtained from a numerical solution is more advantageous compared to those of an experimental visualization, in the sense that diffusion of the tracer in the working fluid does not occur. A set of 10 streaklines, all of them originating upstream from the cylinder, are depicted in Figure 7 at $t/T = 0$. The streaklines are numbered consecutively from 1 to 10, with number 1 being given to the streakline originating from the lowermost point from the cylinder, while number

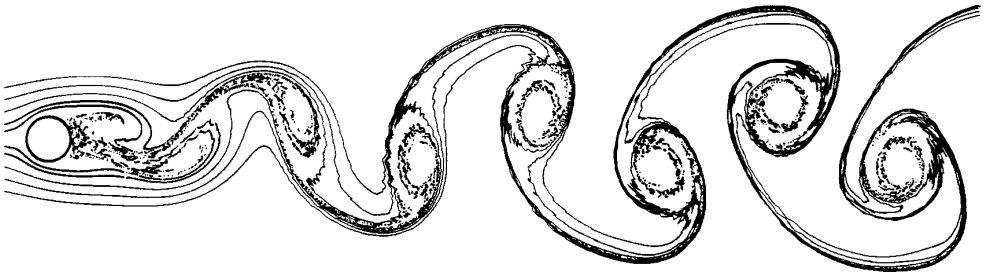

Figure 7. Pattern of ten streaklines in the cylinder wake at $t = 0$.

10 corresponds to that starting from its symmetric point with respect to the wake centreline. Figure 7 gives good insight to the mass transfer process across wake due to vortex shedding. Points emanating from the upper part of the flow field upstream from the cylinder find their way in the lower part of the wake and *vice versa.* In addition, although the streakline pairs which originate farthest from the cylinder are kept at a distance apart in the near wake, they come very close to each other near the outflow boundary. The filament lines 5 and 6 are depicted in Figure 8(a). Figure 8(a) reveals that the lines 5 and 6 are caught in the recirculation region and their constitutive points are superimposed, rendering the two lines indiscriminate, apart from a small length downstream from the cylinder where the two lines can be distinguished. This is the reason for plotting the filament line 6 separately in Figure 8(b). It should be mentioned that the numbering of the vortices in Figures 8(b) and 9 is different from that appearing in the equivorticity contours pattern of Figure 2.

Zdravkovich (1969) using smoke as tracer in air showed a streakline caught up in the recirculation region, in which the vortices show absence of smoke in their centres. The interpretation given by Zdravkovich to the phenomenon is that fluid from one side of the cylinder is contained in the vortices shed from the other side. On the other hand, Gerrard's experiments (1978) in water show clearly the dye injected from one side of the cylinder to accumulate in the vortices of the same side. It is evident from Figure 8(b) that dye injected from one side of the cylinder remains in the vortices of the same side, although it can be found across the wake, but outside the vortex core. The detailed numerical flow visualization conducted by Eaton (1987) favours this argument reasonably. It seems therefore, that either the disturbance level in Zdravkovich's experiments was high leading to spurious results as proposed by Eaton, or the smoke was injected at some distance above the cylinder. In this case a configuration similar to that of Figure 8(b) can be expected, where it is clear that "dye" emerging a small distance above or below the cylinder does not fill the centres of the vortices.

5.2. The Multiple Folding Phenomenon

Figure 8 reveals that the streaklines depicted, after their displacement in the far wake, return to the region behind the cylinder. It is seen from Figure 8(b) for example that the streakline folds around vortex I, then after going as far as vortex II returns to the region behind the cylinder; next it reaches vortex III, afterwards it folds back behind the cylinder, and so on. This situation is similar to figure 8 of Perry *et al.,* where the streaklines emerge from the cylinder surface.

For a better examination of the multiple folding phenomenon of a streakline caught in the recirculation region, the sequences of successive points of the streakline depicted in Figure 8(b) were plotted separately, in a way that the background from the previous foldings was eliminated. The first point of a sequence was indicated by a half arrow, while the last point with a full arrow. The first 1000 points are depicted in Figure 9.1(a). The line folds around vortex I, finds its way towards the vortex core and then moves back to the cylinder. The sequence of the following 500 points is shown in Figure 9.1(b). The points of the line are initially closely spaced, then jump to the crest, fold around vortex II, move back to the crest and return to the position of the full arrow. The sequence of the next 500 points depicted in Figure 9.1(c) moves initially back to the cylinder jumping over the crest, changes direction close to the cylinder trailing edge, and then moves again towards the cylinder. The next point of the sequence is the highest of the frame. Consequently, there exists a large gap between two successive

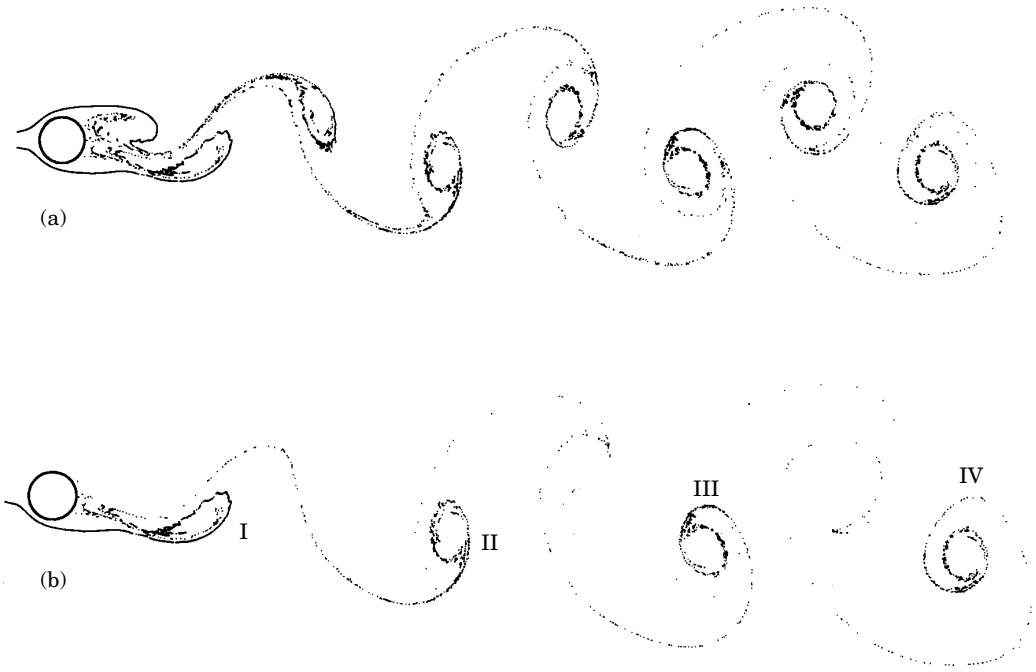

Figure 8. (a) Streaklines 5 and 6; (b) Streakline 5.

points. The next points of this cluster find their way to vortex III, fold back to the position of the lowermost arrow to the right pointing towards the cylinder, and then move back to the vortex core. The next 200 points depicted in Figure 9.1(d) after an initial motion to the downstream direction escape from the region of vortex III and move backwards. The following 100 points shown in Figure 9.1(e) move towards the cylinder, then to the area of vortex I and then they return close to the trailing edge of the cylinder. Afterwards a great jump occurs until vortex IV is reached. The next 300 points depicted in clusters of 100 in Figure 9.2(a–c) wander around the core of vortex IV. The next 100 points of Figure 9.2(d) escape from the core area, move across wake and they return to the core of vortex IV, while the following 50 points, as shown in Figure 9.2(e), perform a similar motion. In Figure 9.2(f) the following 50 points of the streakline escape from the core of vortex IV and find their way close to the cylinder. The next 21 points are depicted in frame 9.3(a). There exist substantial gaps between successive points, some points overlap on each other and the arrows used are inadequate to describe the sequence of the points. The same applies for the last 30 points depicted in Figure 9.3(b). The present computational study confirms the ''finger'' phenomenon described by Gerrard (1978). In Figure 9.1(b) for example there exists a gap between the first points of the sequence and the highest point of the frame, which is filled in Figure 9.1(c) when the line returns to the recirculation region.

From the foregoing discussion on Figure 9 it follows that in some cases there exist significant gaps between consecutive points in this representation of streaklines as a sequence of distinct particles. The reason is that the part of the streakline caught in the recirculation region remains in the area close behind the cylinder for a rather long period as indicated from Figure 9.1(c). This is further substantiated from Figure 9.1(e), in which the particles close to the trailing edge of the cylinder are seen to have been introduced in the flow approximately during the time interval that produced vortex III.

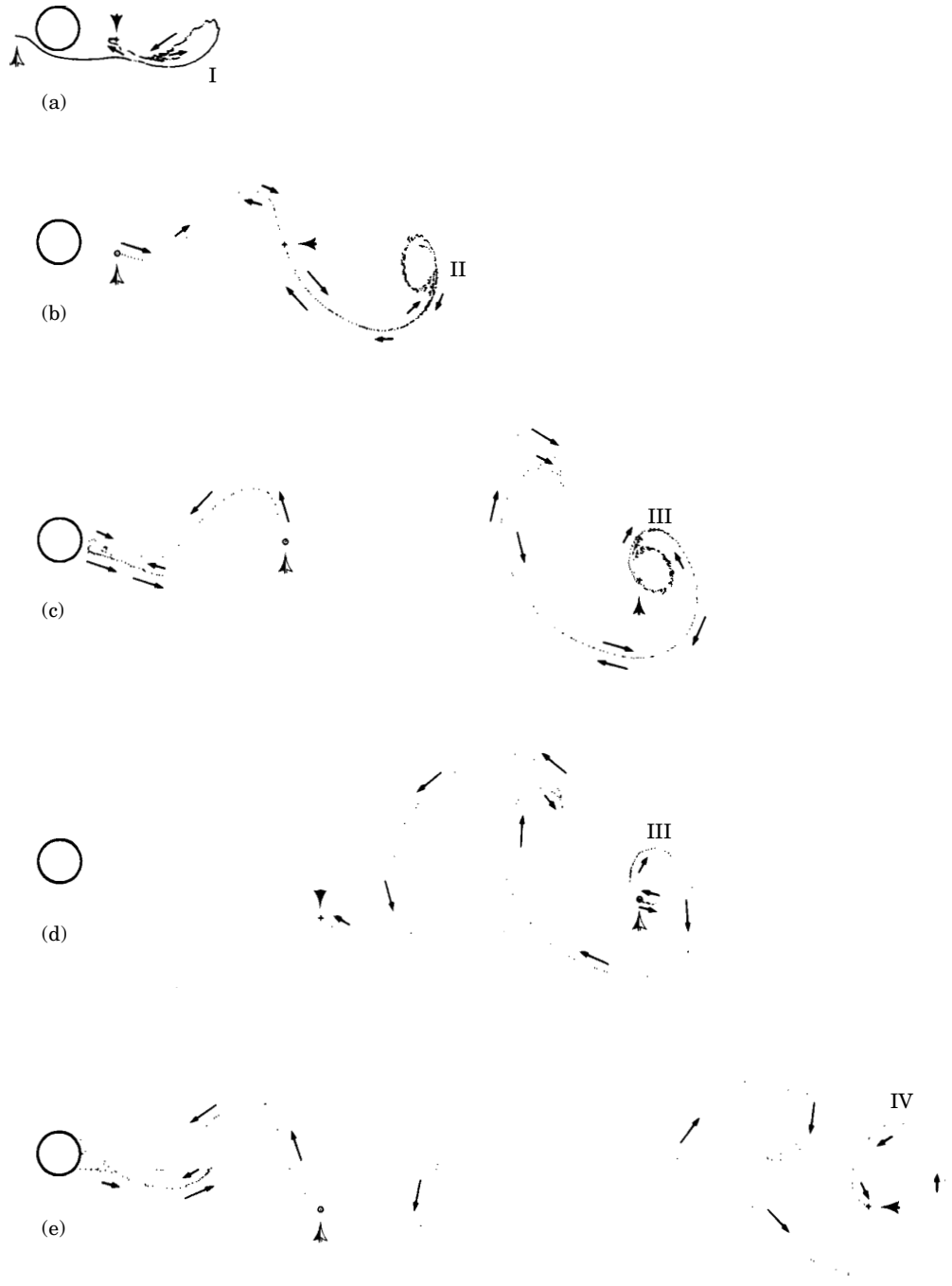

Figure 9.1. Points 1 to 2 200 of streakline 5. (a) Points 1 to 1 000; (b) Points 1 001 to 1 500; (c) Points 1 501 to 2 000. (d) Points 2 001 to 2 100. (e) Points 2 101 to 2 200. The symbol ⍋ denotes the first point of the sequence while the symbol ▲ the last.

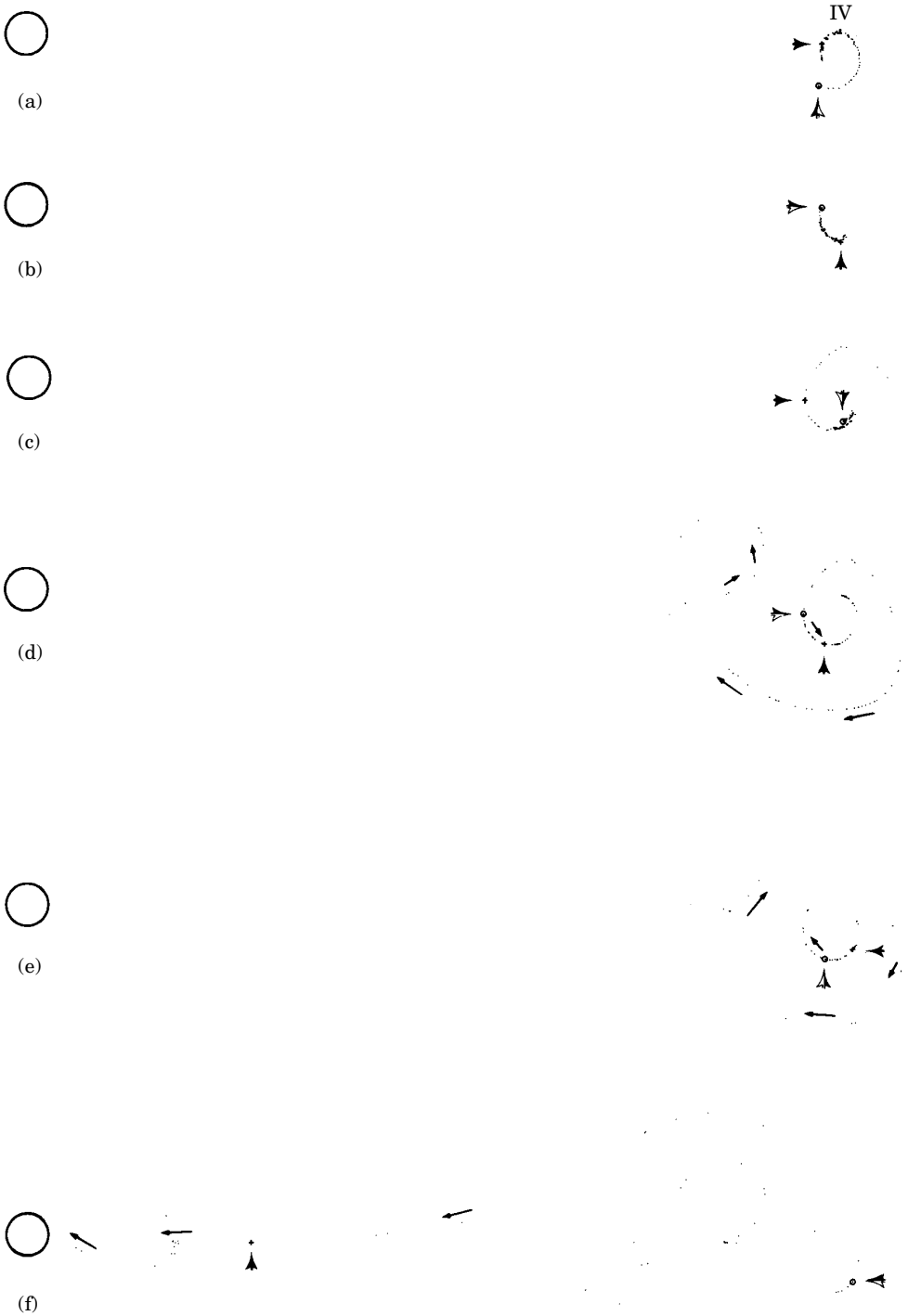

Figure 9.2. Points 2 201 to 2 700 of streakline 5. (a) Points 2 201 to 2 300; (b) Points 2 301 to 2 400; (c) Points 2 401 to 2 500. (d) Points 2 501 to 2 600. (e) Points 2 601 to 2 650. (f) Points 2 651 to 2 700.

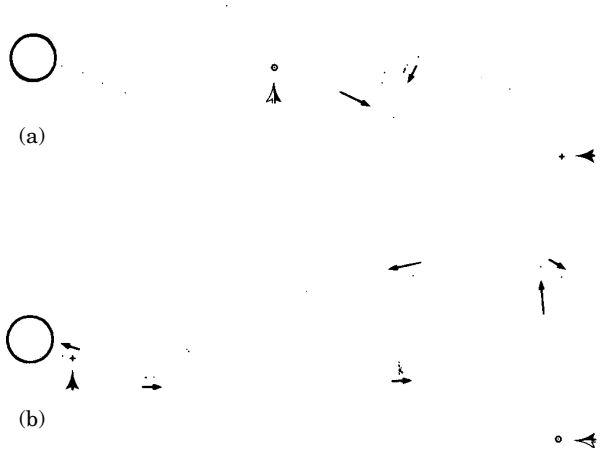

Figure 9.3. Points 2 701 to 2 752 of streakline 5. (a) Points 2 701 to 2 721; (b) Points 2 722 to 2 752.

Figures 8(b) and 9.1(e) demonstrate that some of these particles find their way in the interior of vortex I, which means that the part of the streakline which is caught in the recirculation region is scavenged by successive vortices shed from the same side of the wake. Another conclusion from Figure 9 is that in many cases the sequence of successive points is erratic. In spite of the erratic position of consecutive points, all points are located on the same line, as shown in Figure 8(b). The random position of successive points can be interpreted with reference to Figure 10, where the points are numbered. In Figure 10(a) 21 points (1600 to 1621) of streakline 5 are portrayed as they move from the cross-wake region to the core of vortex III. The same method of numbering was used in order to elucidate the random sequence of some points belonging to the same streakline. The points 2700 to 2721 depicted in Figure 9.3(a) are numbered in Figure 10(b). From Figure 10(b) we can observe the large spacing between consecutive points, for example points 4 and 5, and the very small spacing between others, such as points 6 to 12, which almost overlap.

5.3. Streaklines versus Equivorticity Lines

The pairs of streaklines 3 and 8 and 5 and 6 superimposed on the equivorticity lines throughout the solution domain at $t/T = 0$ are depicted in Figure 11. It is seen that both the equivorticity lines and the streaklines can be used for the determination of the vortex centres. Moreover, when the filament lines approach each other connecting neighbouring vortices of opposite sign, they move along the parts of the minimum vorticity contours farthest from the wake axis, marking locally the boundary between the low vorticity region and the irrotational part of the flow field.

In order to explain the relationship between the streaklines and the equivorticity lines in greater detail, the four streaklines of Figure 11 were superimposed on the equivorticity lines over one half of a shedding cycle in Figure 12. It is very interesting to note that when the streaklines loop around a vortex core, they are superimposed locally on an equivorticity contour. This superposition is maintained as the vortices grow and move downstream. We can assert therefore that if the streaklines originate close enough to the cylinder and recirculate, their points encompassing a vortex centre have approximately the same vorticity. This is further substantiated with reference to Figure 11, where streaklines 5 and 6 around the last three vortices are almost

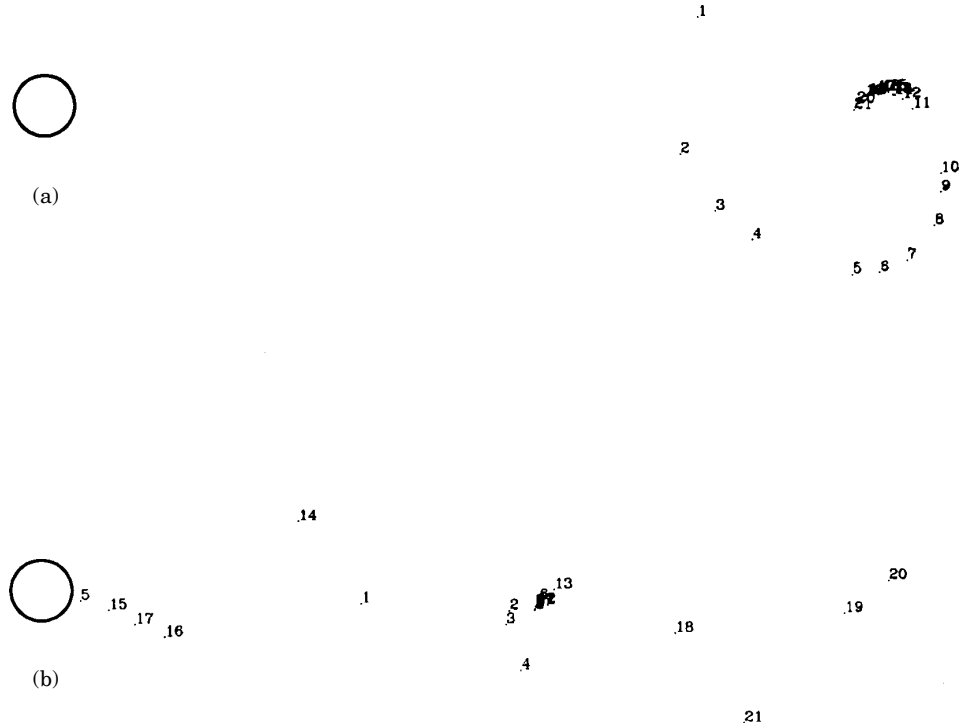

Figure 10. Sequence of clusters of points of streakline 5. (a) Points 1 600 to 1 621; (b) Points 2 700 to 2 721 (same sequence as in Figure 9.3(a)).

superimposed on the vorticity contour of greater absolute vorticity. The superposition of the filament lines on the equivorticity lines also gives an idea about the first appearance of the vortices. In Figure 12(a) a wave in streakline 5 is detectable behind the cylinder, which has been interpreted in the flow visualization study by Gerrard (1978) as the first appearance of the vortices. In Figure 12(b) the local growth of the vortex is accompanied by an increase in the wave appearing in streakline 5. In Figure 12(c) the continuing growth of the vortex with accumulation of almost constant vorticity is detectable, while the wave in streakline 5 has taken the form of a kink; whereas the further concentration of vorticity characterizing a forming vortex and the commencement of rolling-up can be observed in Figure 12(d).

6. THE PRESSURE DISTRIBUTION

6.1. Pressure Distribution Throughout the Flow Field

The isobars throughout the flow field at $t/T = 0$ are presented in Figure 13. The pressure is positive upstream and negative downstream from the cylinder. The centres of the vortices are detectable as minimum pressure contours in the flow field, while the absolute value of pressure in the vortex centre decreases with downstream distance of the vortices. It is interesting to note the regions of very low positive pressure outside the negative pressure region downstream from the cylinder. The pressure distribution presented in Figure 13 is very similar to those inferred from the interferometric study by Green & Gerrard (1991). The high pressure region in the present solution associated with stagnation is in contact with the cylinder, while in the study by Green & Gerrard is displaced in front of the body; the interpretation given by these researchers

Figure 11. Streakline pairs 3–8 and 5–6 superimposed on the equi-vorticity contours at $t = 0$.

is that the displacement of high pressure region upstream is an effect of surface tension and flow over the top of the cylinder. The point of minimum pressure is the centre of the innermost contour closest to the cylinder, which oscillates in value and position.

The isobars close to the cylinder at four time intervals over one half of a shedding cycle are depicted in Figure 14. In Figure 14(a) the minimum pressure contour has the value -1. The regions of low positive pressure are detectable outside the negative pressure region, while a pressure "hill" of still negative pressure starts to develop below the minimum pressure area, in the negative y-axis. In Figure 14(b) the low pressure region behind the cylinder has moved downstream while the innermost contour has acquired the value $-0{\cdot}9$; a new low pressure region starts to develop at the bottom of the cylinder. The high pressure region close to the cylinder has increased in size, while the values of the inner contours have become positive. In Figure 14(c) the low pressure region at the bottom of the cylinder has increased in size, the minimum pressure contour being $-0{\cdot}9$. The positive pressure region has increased still further and is still surrounded by a negative pressure area. Finally, in Figure 14(d) the low pressure region at the bottom of the cylinder has been further increased; the same happens with the positive pressure region closest to the cylinder, which now lies clearly outside the negative pressure region. The pressure contours pattern of Figure 14(a) is in very good agreement with Green & Gerrard's Figure 7(b), although the Reynolds number in Green & Gerrard's experiment was 80. Three vortices are shown in both figures, while the two positive pressure regions shown display remarkable similarity. Green & Gerrard quote the pressure distribution near the cylinder derived numerically by Braza *et al.* (1986) at $\mathrm{Re} = 100$. Comparing Figure 14 with the Braza *et al.* results contained in Green & Gerrard's figure 8, we deduce that there exists considerable agreement between Figure 14(b, d) of the present investigation and Green & Gerrard's figure 8(b, c) which refer to similar instants over a period. A prominent discrepancy between Green & Gerrard's experimental patterns and the results of both numerical solutions is that the low pressure region derived experimentally is very close to the wake axis, while in the computational results appears to be displaced laterally. Possibly this is another effect of surface tension and flow over the top of the cylinder.

6.2. Superposition of Isobars on Equivorticity Lines and Streamlines

The isobars superimposed on the equivorticity lines throughout the solution domain are depicted in Figure 15. It is seen in Figure 15 that the points of maximum absolute value of vorticity coincide with the points of maximum absolute value of pressure; this observation does not apply exactly in the part of the wake close to the cylinder, where a small deviation of the point of maximum absolute pressure from that of maximum

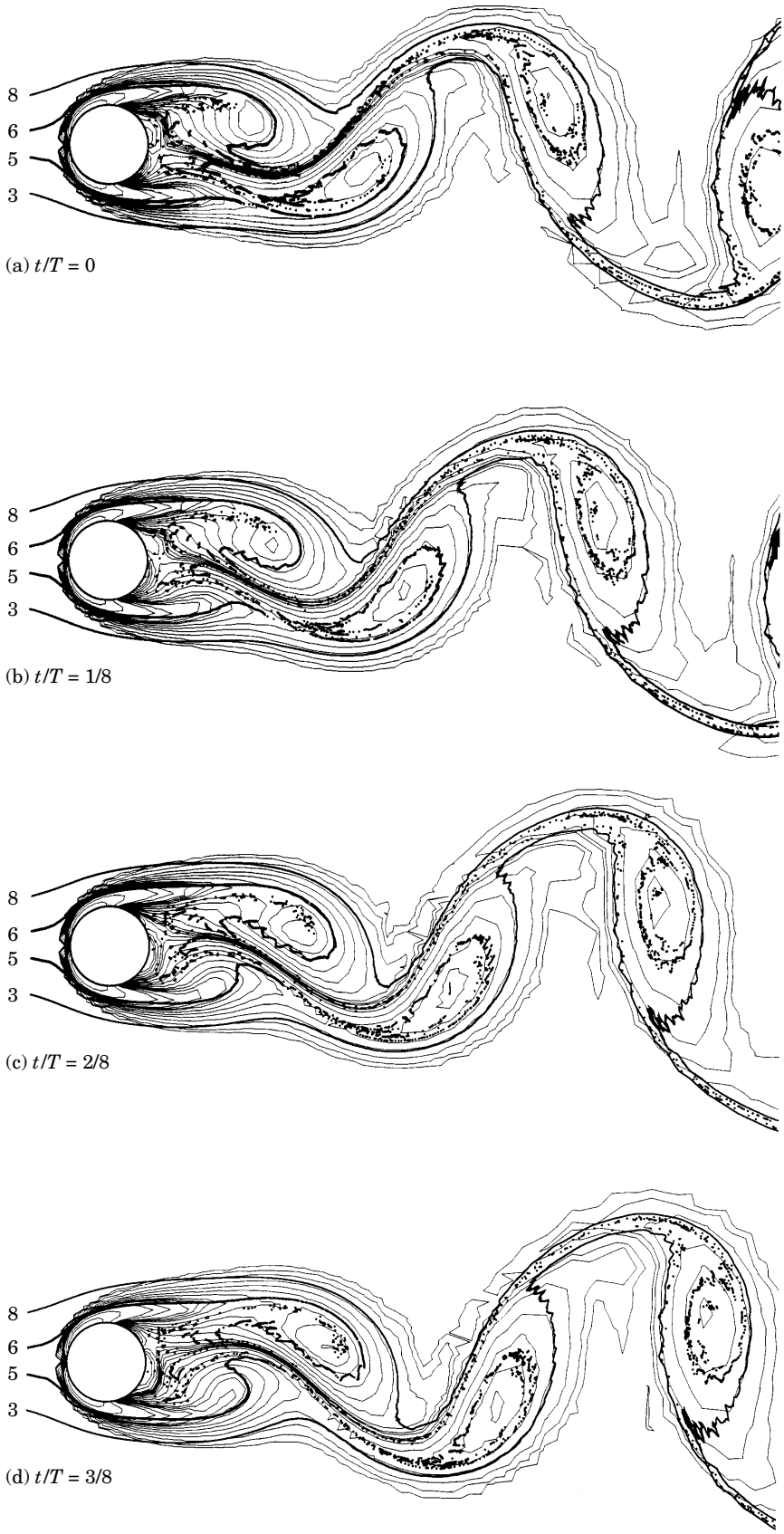

Figure 12. Streakline pairs 3–8 and 5–6 superimposed on the equivorticity contours in the near wake separated by a time interval of $T/8$.

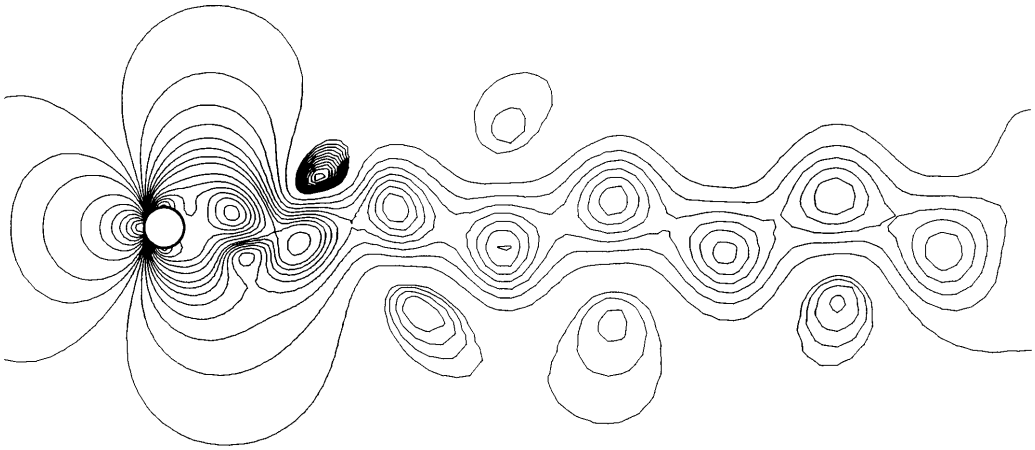

Figure 13. Pressure distribution throughout the domain at $t = 0$.

absolute vorticity is obvious. It can be also seen from Figure 15 that the most distant points from the cylinder of the outermost equivorticity lines of each vortex lie on the minimum pressure lines which originate from the cylinder and extend as far as the outflow boundary. This does not apply exactly to the negative vorticity vortex farthest from the cylinder, and it is possibly an effect of the truncation of the solution domain. An important conclusion from Figure 15 is that in the part of the wake close to the cylinder high pressures prevail where the two parts of an equivorticity line with end points on the cylinder which surrounds a vortex not completely detached approach each other, forming a necking. This is further elucidated with reference to Figure 16, where the equivorticity lines are superimposed on the isobars near the cylinder over a half of a shedding period.

In Figure 16(a) a positive pressure region has already developed in the position where the two opposite parts of the equivorticity lines have come closest above the cylinder, whereas a pressure hill starts to form at the equivorticity line necking underneath the cylinder, the value of the pressure contour being still negative. In Figure 16(b) the high pressure region above the cylinder has increased in size while the pressure values in the inner contours have decreased, displaying a behaviour similar to a diffusion process. Moreover, the high pressure loop is not located at the point of equivorticity line necking any longer, but it has been convected downstream. On the other hand, the high pressure region below the cylinder has increased in size and the pressure in the position of equivorticity line necking has become positive. In Figure 16(c, d) the high pressure region above the cylinder is convected downstream, continuing to display the diffusion behaviour. The high pressure region below the cylinder increases continually, remaining attached to the point of equivorticity line necking. In Figure 16(c) we can detect the final stage of a necking process, where the opposite points of an equivorticity line have coincided, dividing the line in two parts; one attached to the cylinder and another forming a closed loop as part of the vortex-shedding process. In Figure 16(d) the positive pressure region has been extended, and is not surrounded by negative pressure contours any longer.

The isobars superimposed on the streamlines at $t/T = 0$ are depicted in Figure 17. It can be noticed that the point of minimum pressure in the flow field lies on the separatrix which bounds the rotating bulk of fluid from the alleyways drawn across the wake from the lower part of the flow field. Near the cylinder there exist two regions of

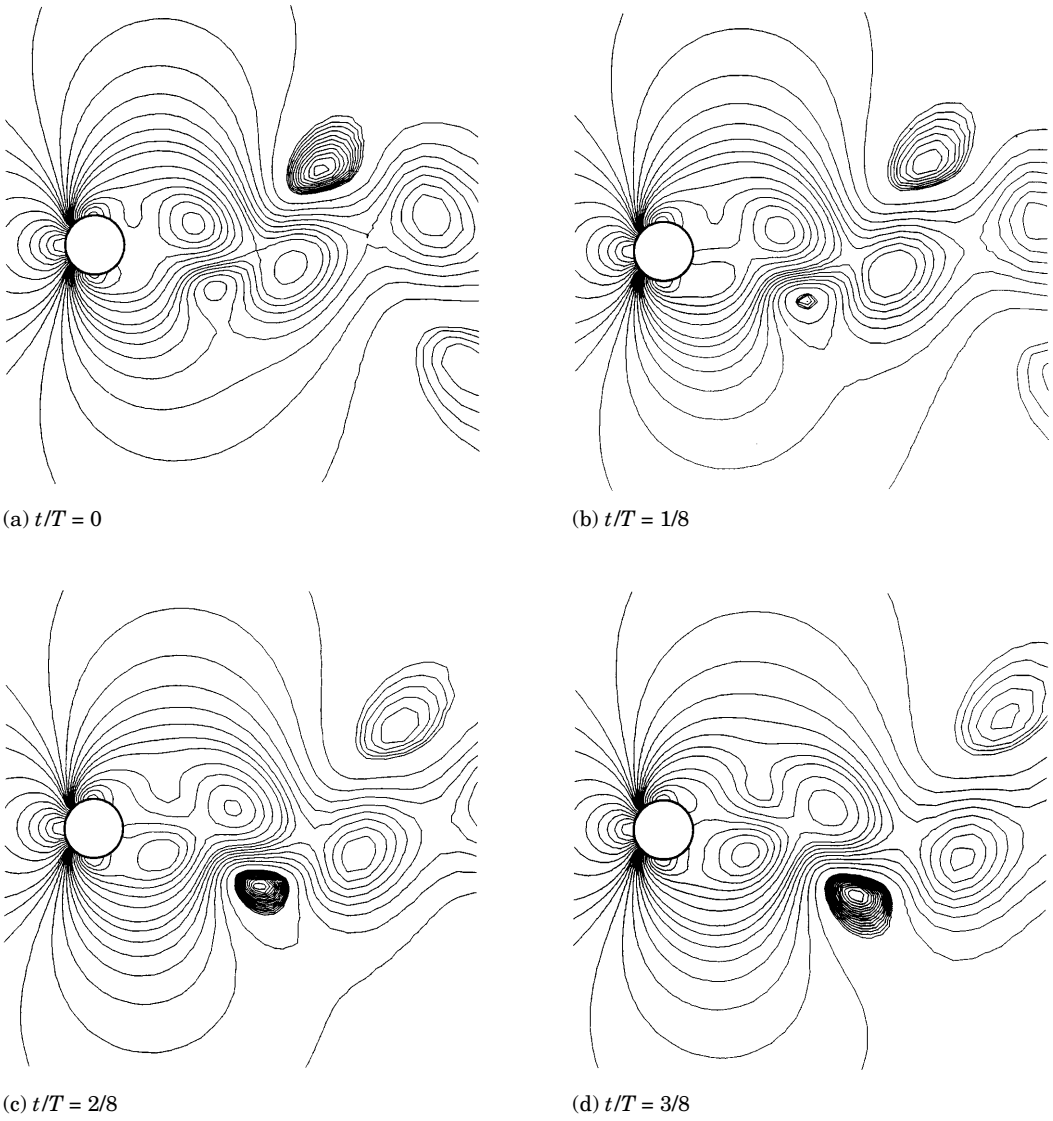

(a) $t/T = 0$ (b) $t/T = 1/8$

(c) $t/T = 2/8$ (d) $t/T = 3/8$

Figure 14. Isobars in the near wake separated by a time interval of $T/8$.

locally higher pressure. The first is located behind the top of the cylinder, where the alleyways drawn from the bottom come close to the cylinder; the second appears under the cylinder where the distance between the two opposite parts of an equivorticity line becomes minimum, as already explained. Moreover, the pressure becomes minimum at the vortex centres, which are defined by the maximum lateral displacement of the stagnation streamline.

7. FLUID VELOCITIES

The fluid velocities are not computed directly from this stream function and vorticity numerical scheme, but they are calculated from the nodal values of the stream

Figure 15. Equivorticity contours shown together with the isobars at $t = 0$. The thick lines represent the equivorticity contours.

function. The calculation of the two components of the fluid velocity throughout the computational domain is necessary for the computation of pressure from Poisson's equation. Velocity traces in the streamwise direction were available from an experimental investigation, and the comparison with the computed values would be a useful verification of the accuracy of the numerical solution. The experiments were carried out in a water channel 60 cm wide by 70 cm deep, located in the Department of Aeronautics at Imperial College, London, as part of a more general project, also comprising velocity measurements in the wake of a vortex-excited cylinder. The results for the oscillating cylinder case have been presented by Anagnostopoulos & Bearman (1992) and Anagnostopoulos (1994). Hot film anemometers were used for the measurement of the fluid velocity in the streamwise direction, at $\mathrm{Re} = 115$. The difference between the Reynolds number used in the computation and that of the experiment can be ignored from the following argument. In the numerical solution, due to the proximity of the solid boundaries, the corrected freestream velocity from formula (1) is higher than the theoretical by a factor of 1·018, increasing the effective Reynolds number by the same ratio. Moreover, the numerical model is two-dimensional while the vortices in the experiment are shed at a slanted angle, having as effect the reduction of the Strouhal number with respect to the parallel shedding value, as will be explained later. The combined effect of the two previous reasons is the great proximity of the Reynolds number in the computation and the experiment, which is verified from the shedding frequencies. The computed shedding frequency was 6·84 Hz while it was 7 Hz in the experiment, their difference being only 2%.

The computed values of the streamwise fluid velocities superimposed on the measured ones at the same points of the flow field are depicted in Figure 18. The agreement between numerical and experimental values is very good, providing good evidence of the accuracy of the numerical solution. The greatest discrepancy appears close to the cylinder, while farther in the wake the difference is so small that the computed traces are hardly distinguishable under the experimental velocity traces. It seems therefore that the effects of the small difference between the Reynolds numbers in the computation and in the experiment are confined in a small region behind the

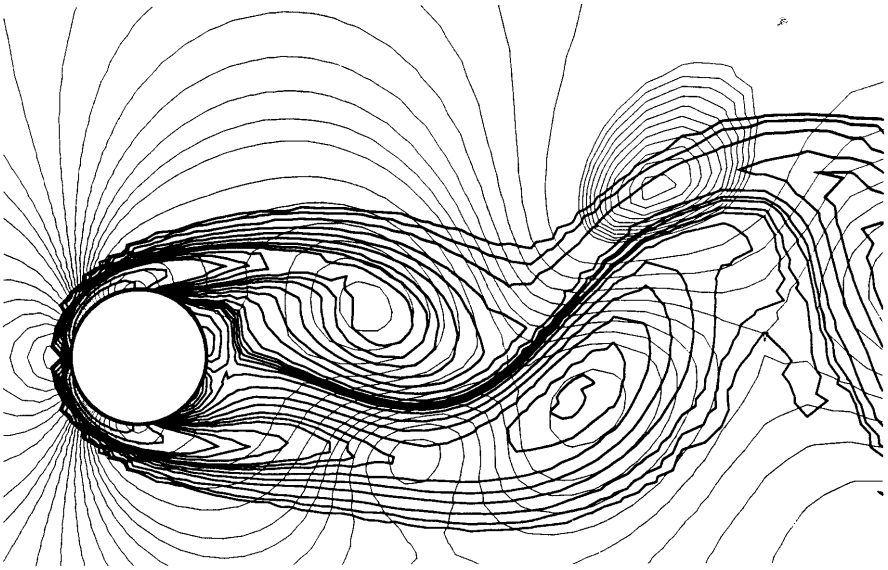

(a) $t/T = 0$

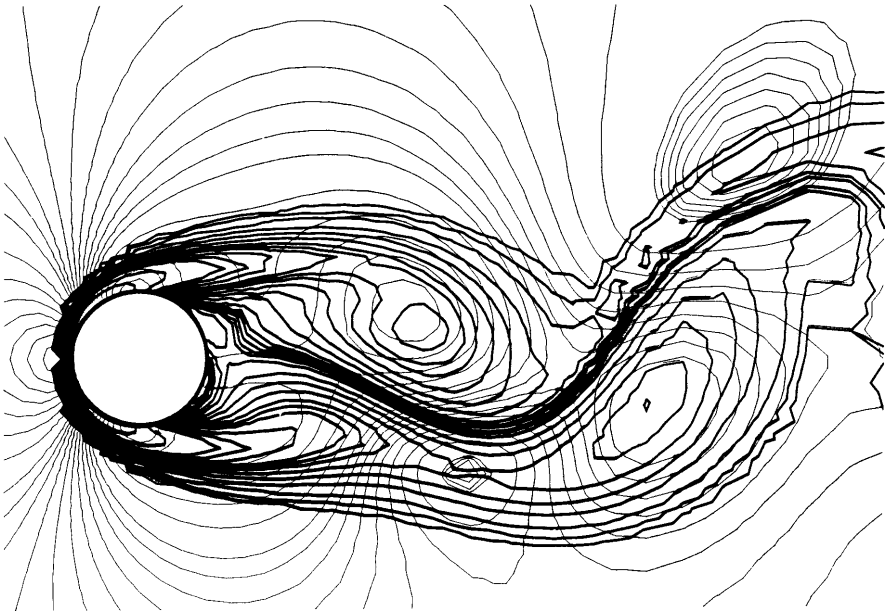

(b) $t/T = 1/8$

Figure 16. Equivorticity contours (thick lines) superimposed on the isobars (thin lines) in the near wake separated by a time interval of $T/8$.

cylinder. In all traces of Figure 18 the fundamental frequency at which the vortices are shed is detected, together with the first harmonic. For the same longitudinal distance downstream, the effect of the first harmonic decreases with increasing distance from the wake axis.

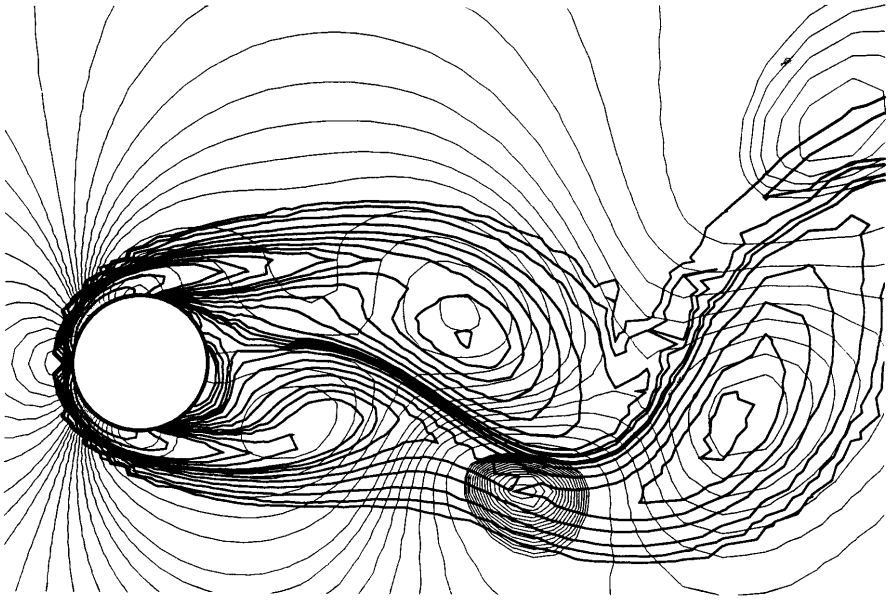

(c) $t/T = 2/8$

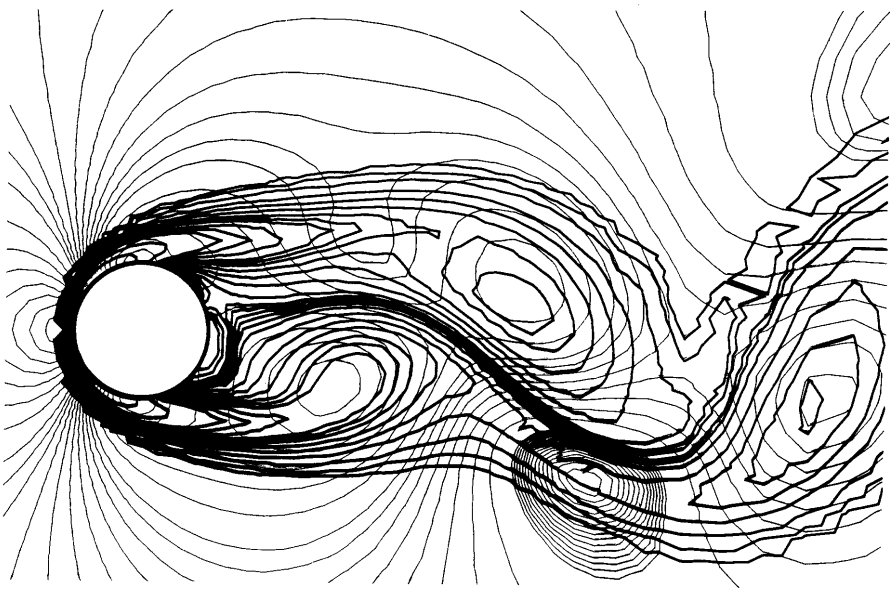

(d) $t/T = 3/8$

Figure 16. (*Continued.*)

Traverses of the mean streamwise velocity over a period at three different locations along the wake axis are portrayed in Figure 19. An interesting feature of Figure 19 is that the velocity on the wake axis at $x/d = 9{\cdot}25$ is higher than that at $x/d = 6$, but the velocity on the wake axis at $x/d \times 14{\cdot}5$ is lower than both previous values. Figure 19

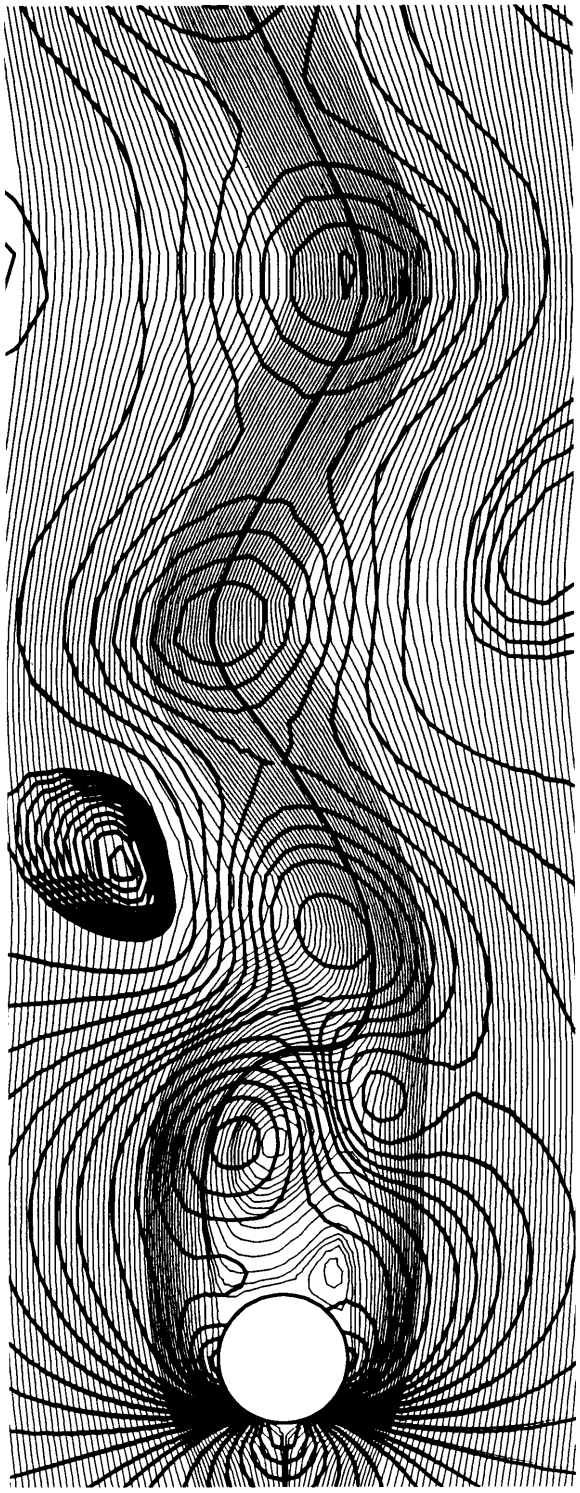

Figure 17. Pressure distribution over the streamline pattern at $t = 0$.

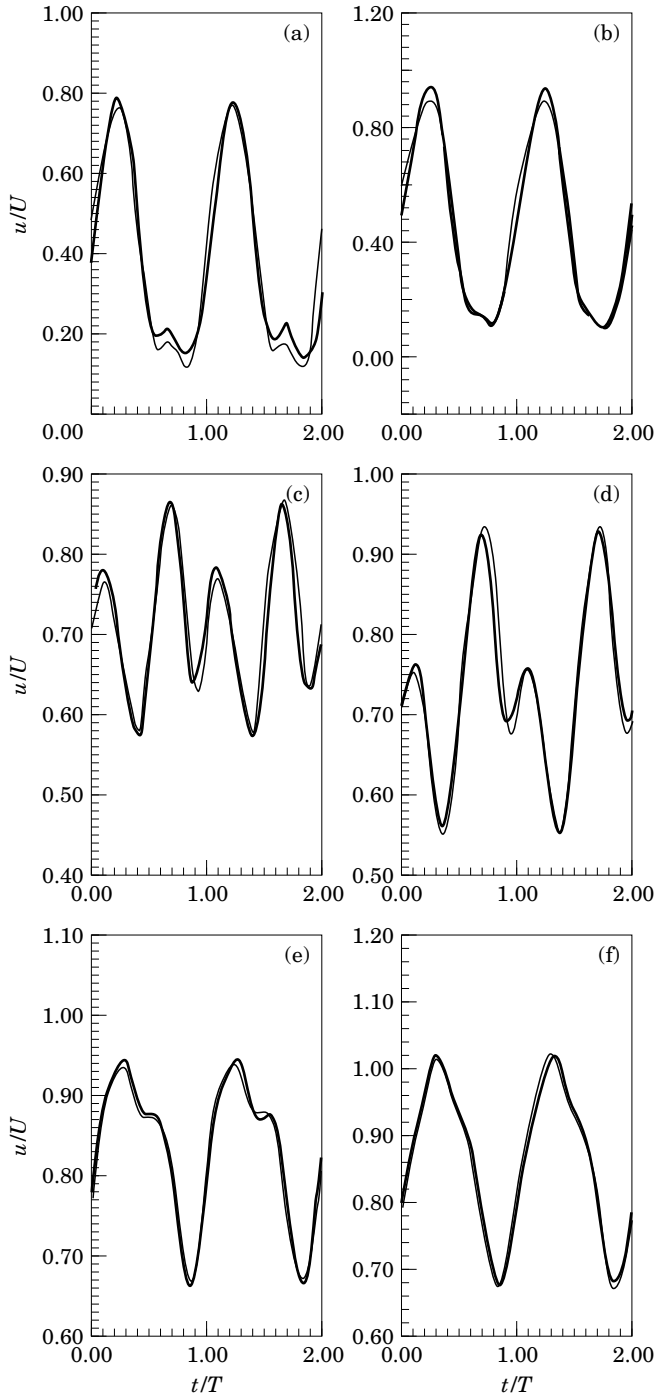

Figure 18. Computational (thin lines) and experimental (thick lines) streamwise velocities of the fluid as functions of time. (a) $x/d = 2{\cdot}70$, $y/d = 0{\cdot}32$; (b) $x/d = 2{\cdot}70$, $y/d = 0{\cdot}43$; (c) $x/d = 4{\cdot}90$, $y/d = 0{\cdot}17$; (d) $x/d = 4{\cdot}90$, $y/d = 0{\cdot}33$; (e) $x/d = 7{\cdot}50$, $y/d = 0{\cdot}5$; (f) $x/d = 7{\cdot}50$, $y/d = 0{\cdot}75$.

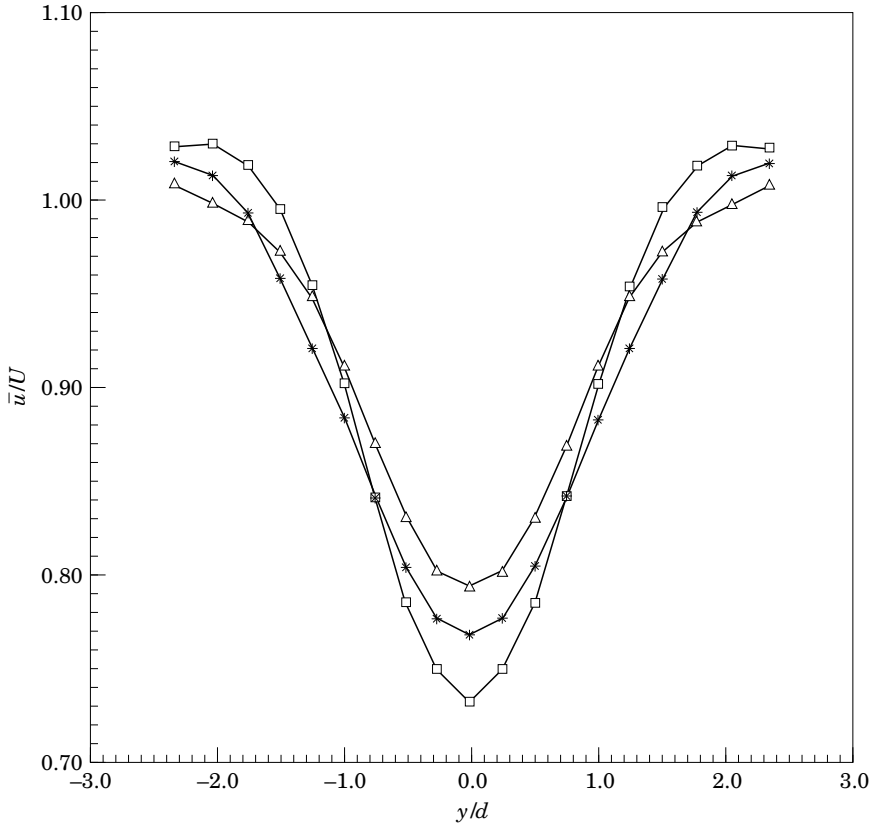

Figure 19. Traverses of the average streamwise velocity of the fluid over a period: —*—, $x/d = 6{\cdot}0$; —△—, $x/d = 9{\cdot}25$; —□—, $x/d = 14{\cdot}5$.

confirms the continuity principle according to which high velocity near the wake axis has as effect the reduction of velocity at some lateral distance from the centreline of the wake and *vice versa.* The average velocities over one period on the wake axis are depicted in Figure 20, which reveals that the minimum value occurs at $x/d = 1{\cdot}5$; then the mean velocity increases abruptly until it reaches its maximum value at $x/d = 8$, and decreases mildly until the outflow boundary is reached. The r.m.s. value of the streamwise velocity fluctuation u' on the wake centre line is shown in Figure 21. The point of the maximum $u'_{\text{r.m.s.}}$ is one of the criteria for the determination of the vortex formation length. Figure 21 shows that the maximum r.m.s. value of the u velocity fluctuation occurs at $x/d = 3{\cdot}05$ and is lower than one-tenth of the freestream velocity.

The peak to peak fluctuation of the transverse fluid velocity over a cycle on the wake axis is displayed in Figure 22. It should be remembered that due to the symmetry of the mean flow with respect to the wake axis, the mean v velocity is zero. Contrary to streamwise velocities, the transverse components do not appear frequently in the literature. The computational work by Anagnostopoulos (1994) has shown that only the fundamental frequency is detectable in the lateral velocity trace over a period and the differences at various points in the transverse direction are small. Green & Gerrard (1993) quote that for $\text{Re} = 100$ at $x/d = 1$, $v'_{\max}/U = 0{\cdot}23$. This is exactly the value

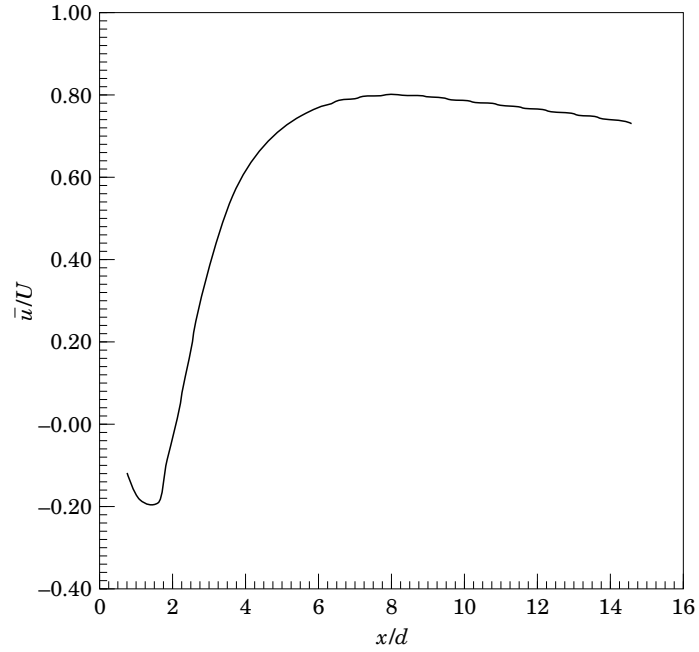

Figure 20. Distribution of the average streamwise velocity over a period along the wake axis.

derived from the present computation as follows from Figure 22, considering that the v'_{max} values shown are peak to peak. It should also be stressed that the maximum v' amplitude on the wake axis occurs at $x/d = 3{\cdot}05$, which is the location where the $u'_{r.m.s.}$ over a period becomes maximum.

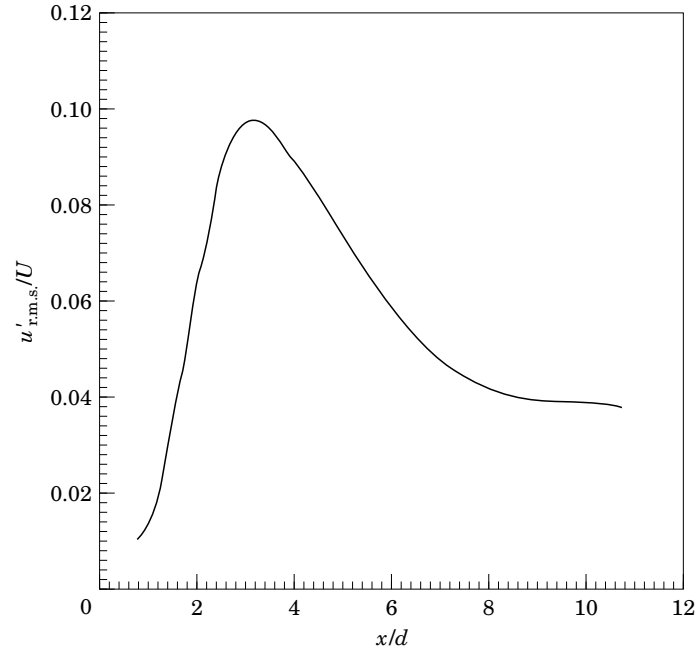

Figure 21. Distribution of the r.m.s. streamwise velocity over a period along the wake axis.

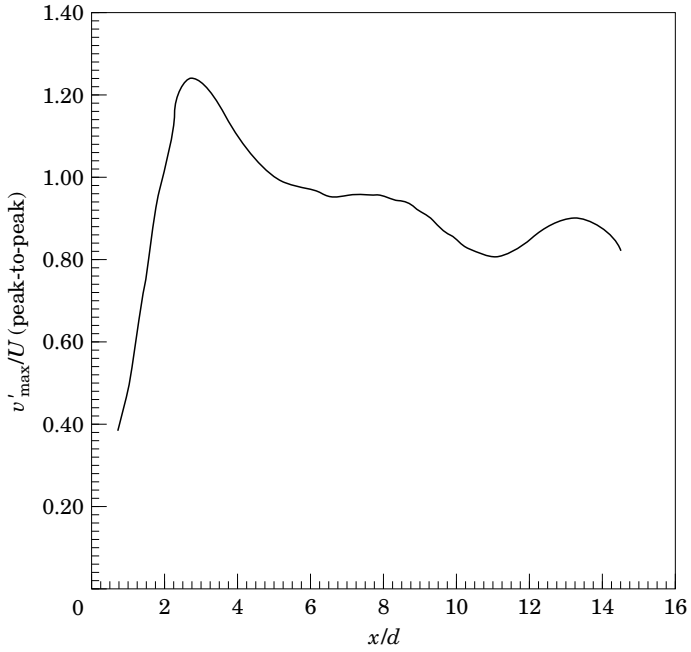

Figure 22. Distribution of the transverse velocity fluctuation over a period along the wake axis.

8. PARAMETERS OF WAKE GEOMETRY

The most important parameter of the vortex street wake geometry is the ratio of longitudinal to lateral spacing in the "stable region", where the vortices shed from the two parts of the cylinder move along two parallel lines and their spacing ratio is constant as they are convected downstream. Both the equivorticity and the filament lines (Figures 2 and 7) display a vortex street whose geometry remains constant as far as the outflow boundary. The longitudinal spacing, α, is $5{\cdot}437d$ and the lateral spacing, β, is $1{\cdot}44d$, yielding a spacing ratio $\beta/\alpha = 0{\cdot}264$, very close to von Kármán's inviscid theory value, which is 0·281. Schaefer & Eskinazi (1959) report at $\mathrm{Re} \approx 100$ that $\alpha/d = 5{\cdot}30$ and $\beta/d = 1{\cdot}30$, which give a lower spacing ratio $\beta/\alpha = 0{\cdot}24$.

The convective velocity of the vortices U_c is 0·0595 m/s, the ratio U_c/U being 0·901 and the shedding frequency 6·84 Hz, yielding a dimensionless Strouhal number 0·1658. Gerrard (1978) presented the Strouhal number as a function of the Reynolds number as obtained by numerous experimental investigations and fitted polynomials to the frequency variations. Gerrard's (1978) figure 3 reveals a remarkable scatter of Strouhal number values at this range of low Reynolds numbers. The discrepancy of experimental data at this range of low Reynolds numbers was attributed to differences in experimental conditions, accuracy of measurement and different shedding modes. Although the oblique shedding of vortices in the spanwise direction had been detected many years ago, it was not before 1989 when it was stated clearly by Williamson that the Strouhal number, S_θ, for oblique shedding at angle θ is lower than that for parallel shedding S_o, and the oblique shedding data can be collapsed onto the parallel shedding by the transformation $S_o = S_\theta/\cos\theta$. More recently, Williamson (1991), by placing end

plates on the cylinder inclined at a suitable angle, obtained parallel shedding in the spanwise direction. The superposition of Strouhal number as a function of the Reynolds number for parallel shedding and for oblique shedding corrected from the transformation described before, displayed excellent agreement. The Strouhal number value for parallel shedding at $\mathrm{Re} = 106$ according to Williamson (1991) was 0·166, equal to the value of the present solution.

8.1. The Formation Length

An important parameter of the vortex street wake geometry is the length of the formation region. It is generally accepted that the end of the vortex formation region can be defined in the following mutually compatible ways.

(1) The minimum mean pressure on the wake axis (Roshko 1954).

(2) The maximum intensity of the r.m.s. value of the streamwise velocity fluctuation at twice the shedding frequency on the wake axis (Bloor & Gerrard 1966).

(3) The minimum transverse spacing of the regions of maximum r.m.s. streamwise velocity fluctuation (Schaefer & Eskinazi 1959; Bearman 1965). At low Reynolds numbers, according to Schaefer & Eskinazi, this is equivalent to the point where the lateral displacement of the vortices becomes minimum.

(4) The maximum intensity of the r.m.s. value of the longitudinal velocity fluctuation at the shedding frequency off the wake axis (Bearman 1965; Nishioka & Sato 1978).

(5) The point closest to the cylinder at which irrotational fluid crosses the wake axis producing a velocity fluctuation characteristic of the vortex street (Bloor 1964).

The results of the formation length as a function of the Reynolds number found by different investigators are summarized by Green & Gerrard (1993). The main conclusions drawn from this superposition, is that, in the range of Reynolds numbers considered, the formation length decreases with the Reynolds number and there sometimes exist serious discrepancies between different investigations, even for the same definition of the formation length. Bloor and Gerrard (1966) suggested intuitively that the end of the formation region may be the point at which the vortices are strongest. Many years later Green & Gerrard (1993) confirmed from vorticity measurements in the near wake that the position of maximum vertex strength marks the end of the formation region. The distance of the end of the formation region from the trailing edge of the cylinder at $\mathrm{Re} = 100$ was found by Green & Gerrard to be equal to 2·65 cylinder diameters.

The average pressure coefficient over one shedding cycle on the wake axis is depicted in Figure 23. The minimum average pressure occurs at a distance $x/d = 1{\cdot}5$ from the cylinder centre. On the same figure is also plotted the pressure distribution on the wake axis at the instant $t/T = 0{\cdot}475$, which is the time when the minimum pressure appears on the wake axis over a shedding period. The position of minimum pressure on the wake centreline occurs also at $x/d = 1{\cdot}5$ from the cylinder centre, which is the reason for the low mean pressure over a period locally. The isobars around the cylinder at $t/T = 0{\cdot}475$ are shown in Figure 24. The low pressure region is clearly seen below the cylinder in the form of closed loops, which have as effect the pressure drop on the wake axis. It is also interesting to observe in Figure 23 the pressure minima at $t/T = 0{\cdot}475$, which correspond to the longitudinal distance of the centres of the vortices, whereas the pressure maxima correspond to the "saddles" which connect neighbouring vortices of opposite sign. The distribution of the r.m.s. value of the streamwise velocity fluctuation along the wake axis has been presented in Figure 21. The maximum r.m.s.

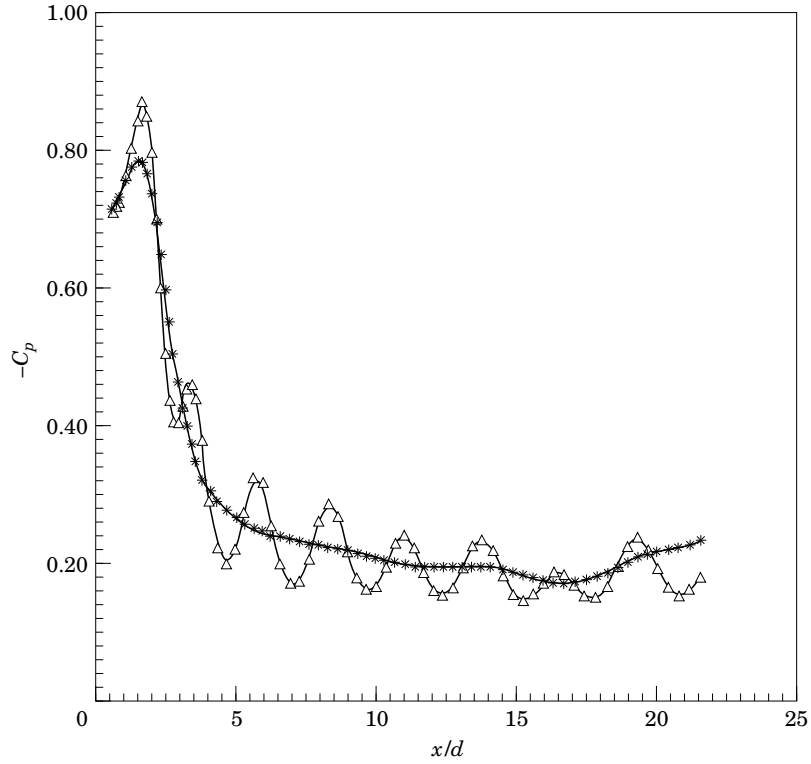

Figure 23. Pressure coefficient along the wake axis: —△—, $t/T = 0{\cdot}475$; —*—, average pressure.

value, equal to 9·8% of the freestream velocity, occurs at $x/d = 3{\cdot}05$ from the cylinder centre, substantially farther downstream from the point of minimum mean pressure.

The lateral displacement of the vortices can be evaluated from the equivorticity lines. From the sequence of equivorticity lines of Figure 3 it is deduced that the minimum lateral displacement from the wake axis, equal to $0{\cdot}19d$, occurs at $t/T = 1/4$, the longitudinal distance of the vortex centre from the cylinder centre being $2{\cdot}38d$. This is the time instant at which the lift force acting on the cylinder becomes minimum. Traverses of $u'_{\text{r.m.s.}}$ at some locations around the position of minimum lateral displacement of the vortices are depicted in Figure 25. It is clearly seen that the minimum distance of the maximum intensity of $u'_{\text{r.m.s.}}$ from the wake axis occurs at $x/d = 2{\cdot}42$, almost coincident to the position of minimum lateral displacement of the vortices. According to Schaefer & Eskinazi (1959) the position of maximum intensity of $u'_{\text{r.m.s.}}$ at a specified longitudinal location is very close to the edge of the vortex core farthest from the wake centreline. At $x/d = 2{\cdot}42$, a simple subtraction of the lateral vortex diaplacement ($0{\cdot}19d$) from the outer viscous core edge ($0{\cdot}43d$) yields the radius of the viscous core, equal to $0{\cdot}24d$. It should be stressed that unlike in the experimental investigations where velocity can be measured at any point in the flow field, the calculation of the fluid velocities in a numerical solution is possible only at the nodal points of the computational grid network. Figure 25 reveals the steep gradients of $u'_{\text{r.m.s.}}$ around its maximum intensity, therefore the accuracy of measurement of this quantity across wake depends on the distance between adjacent nodal points in the cross-flow direction.

For the determination of the point closest to the cylinder at which dyed or

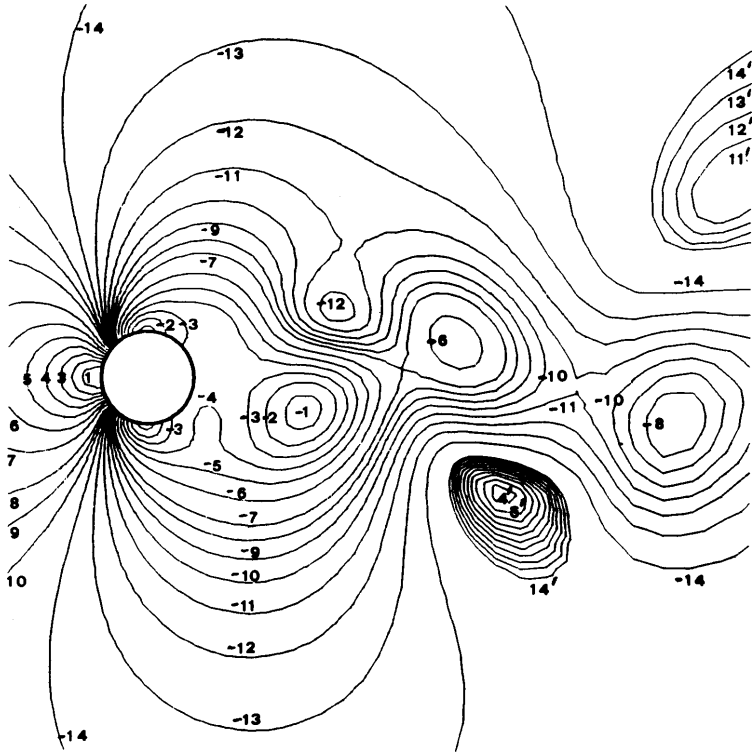

Figure 24. Isobars in the near wake at $t/T = 0{\cdot}475$, and pressure contour numbers.

irrotational fluid crosses the wake axis it is useful to refer to Figure 12, where the streaklines are superimposed on the equivorticity lines. In Figure 12(a) the streakline numbered 6 has just crossed the wake centreline, the distance between the trailing edge of the cylinder and the point of the streakline closest to the cylinder being one diameter, equal to the value quoted by Gerrard (1978). At the point where streakline 6 crosses the wake axis, high vorticity prevails, while the sequence of frames in Figure 12 shows the dye approaching from the downstream direction and not from the upper side, due to the curvature of the streakline. It should also be recalled that the streakline waviness marking the first appearance of the vortices occurs at a distance equal to 1·5 diameters from the cylinder centre. Figure 12(a) shows clearly the indentation of streakline 5 below the cylinder being at the same distance from the cylinder centre as the point where streakline 6 crosses the wake centre line closest to the cylinder. Streakline number 8 has just crossed the wake axis in Figure 12(b). The distance at which streakline 8 crosses the wake axis closest to the cylinder from the cylinder centre is 3·1 cylinder diameters. Moreover, although the vorticity at the point where streakline 8 crosses the wake centreline is low, the fluid is not absolutely irrotational. Irrotational fluid crosses the wake axis closest to the cylinder in Figure 12(d), at a distance equal to 4 cylinder diameters from the cylinder centre. It seems therefore that the point closest to the cylinder at which dyed fluid crosses the wake axis indicates only the beginning of shedding, as reported also by Green & Gerrard (1993).

From the foregoing discussion it is evident that we should distinguish between two different quantities, the length of the first appearance of the vortices and the formation length. The manifestation of the first appearance of the vortices at a distance equal to

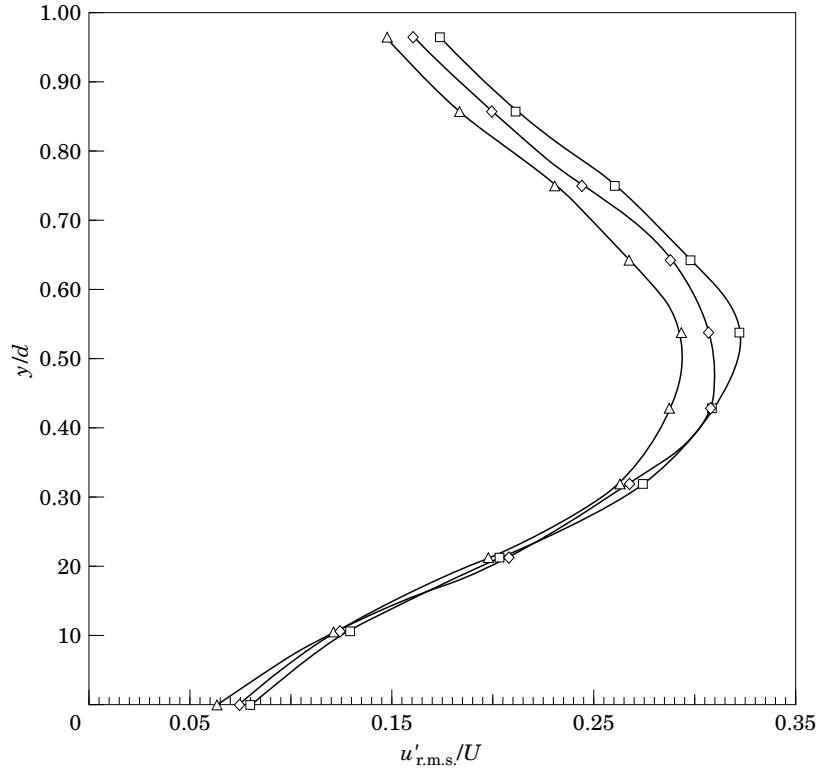

Figure 25. Traverses of the r.m.s. streamwise velocity over a period: △, $x/d = 2{\cdot}26$; —◇—, $x/d = 2{\cdot}42$; —□—, $x/d = 2{\cdot}58$.

1·5 cylinder diameters from the cylinder centre is the accumulation of vorticity of approximately constant magnitude accompanied by a wave locally in a streakline. Moreover, this is the point where the mean streamwise velocity and the mean pressure over a shedding period become minima. Incidentally, this is the distance where dyed fluid emanating near the cylinder crosses the wake axis for the first time. The formation length which marks the end of the formation region is the distance from the cylinder centre where the strength of the vortices becomes maximum, as it can be clearly seen by recalling Figure 6. This is the point where the r.m.s. value of the streamwise velocity on the wake axis becomes maximum, and where the fluctuation of the transverse velocity on the wake axis also becomes maximum. The end of the formation region was found 3·05 cylinder diameters from the cylinder centre, very close to the value reported by Green & Gerrard at $\mathrm{Re} = 100$. The sitation when the vortex centre has just exceeded the formation length is depicted in Figure 16(a). The vortex shedding from the bottom of the cylinder has been separated from the vorticity remaining close to the cylinder, whereas the equivorticity contour stranding the vortex exhibits a narrowing which determines the vortex boundary. The local increase of pressure at the point of vortex boundary is also visible. In Figure 16(d) the centre of the vortex shedding from the top of the cylinder has not reached the formation length yet. The development of a higher pressure region is visible, but it is still displaced towards the cylinder and does not define the vortex boundary. Thus the definition of the formation length is further supported from flow visualization. When the centre of a vortex reaches the formation length, it displays the characteristics of a fully formed vortex. The vorticity and pressure

distribution define in a certain way its boundaries from the vorticity remaining near the cylinder.

8.2. Velocity and Displacement of newly Formed Vortices

The vortices after formation accelerate continuously until they acquire a constant convective velocity. Gerrard (1978) discovered experimentally a transition at $\mathrm{Re} \approx 100$ in the time required for a vortex to obtain the constant velocity. At Re slightly lower than 100, the time required by a vortex from its first appearance to reach constant velocity was approximately half of a shedding period, while at Re just over 100 it was increased to about one period. At $\mathrm{Re} \approx 100$ the time during which the vortex accelerated was very scattered, indicating that the transition is not well defined. There also exists a transition in the distance moved by the vortex from its first appearance to the position where its velocity becomes constant at Re around 100, associated with the time interval of the acceleration. Eaton (1987) calculated the velocity of the vortices as they move away from the cylinder from the streakline configuration. In the present context the equivorticity lines were used for the determination of the centres of the vortices. The equivorticity lines separated by a time interval equal to $T/100$ were generated and the displacement of the vortex under consideration was calculated, while its division by this interval yielded the instantaneous vortex velocity. As $t = 0$ the time of the first appearance of the vortices was considered. The vortex velocity, V, normalized by the constant convective velocity, U_c, as a function of time is depicted in Figure 26. It is recalled that U_c is 90·2% of the freestream velocity, U. The vortex velocity starts from a value as low as 20% of U_c and becomes equal to the constant velocity U_c after 1·3 shedding periods. An interesting observation is that, in the interval between 25% and 45% of a shedding period, the velocity, V, remains constant. From

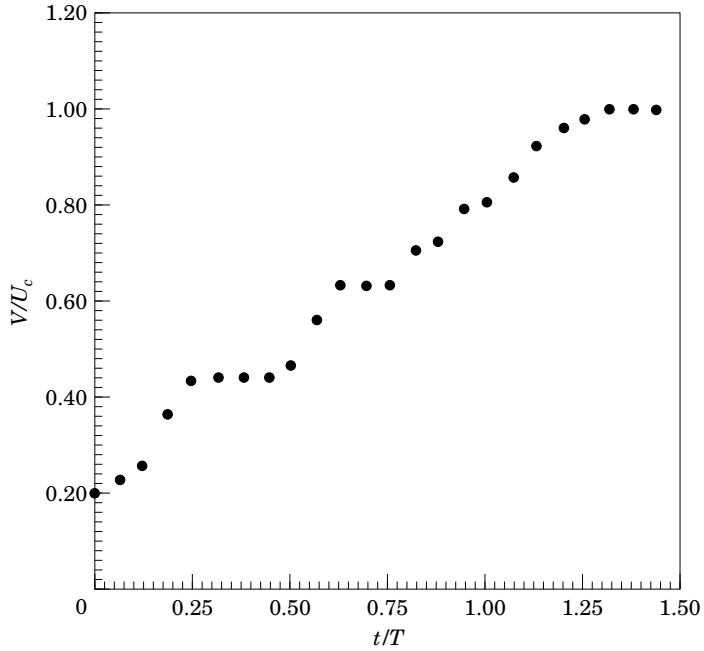

Figure 26. Time-dependent convective velocity of a vortex.

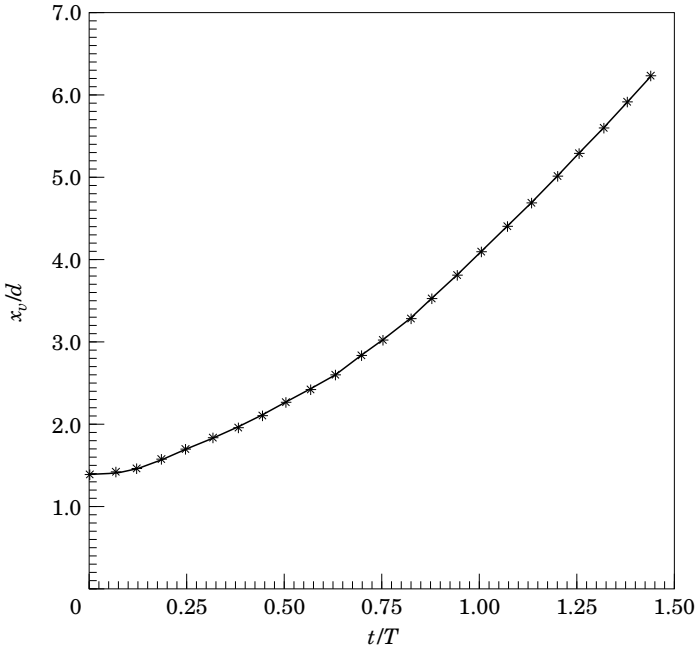

Figure 27. Location of a forming vortex from the centre of the cylinder as function of time.

Figure 27 it is deduced that the vortex acquires constant velocity at a distance x_v equal to 5·6 diameters behind the cylinder centre, or 4·2 diameters from its first appearance; the distance moved by the vortex from its first appearance to the position where its velocity becomes constant corresponds to 75·5% of the longitudinal spacing of vortices. The result obtained herein corresponds to the highest limit of the values quoted by Gerrard (1978).

9. CONCLUSIONS

The finite element method was used for the solution of the two-dimensional Navier-Stokes equations at $\mathrm{Re} = 106$. Computer-aided flow visualization techniques were employed for the generation of streamlines, equivorticity lines, filament lines and isobars. For a better interpretation of the flow characteristics, different flow visualization patterns obtained at the same time instant were superimposed on the same diagram. The superposition of equivorticity lines on the streamline pattern gives insight to the vortex splitting behind the cylinder due to the alleyways drawn across wake, while the presentation of equivorticity lines and isobars on the same diagram reveals the formation of pressure hills at the vortex boundaries. The geometry of the vortex street wake derived from the present numerical study agrees well with flow visualization results of numerous experimental investigations. The streaklines which originate close to the wake axis and are caught in the recirculation region appear to have substantial gaps, while, to a great extent, the sequence of their constitutive points is erratic.

The present computational solution confirmed the result derived experimentally by Green & Gerrard (1993), that the end of the formation region coincides with the position of the vortex centre at which the vortex strength becomes maximum. This is the location where the intensity of the r.m.s. streamwise velocity fluctuation and the

fluctuation of the transverse velocity on the wake axis acquire maximum values. It is remarkable that, when the vortex centre reaches the formation length, the flow visualization patterns depict the initial stage of a fully formed vortex. The point of the first appearance of the vortices can be characterized as the position where the mean longitudinal velocity and the mean pressure on the wake axis become minimum. The position of the minimum transverse spacing from the wake axis of the maximum r.m.s. streamwise velocity fluctuation coincides with that corresponding to the minimum lateral spacing of the vortices. The exact calculation of the amount of circulation shed into the wake during one period verified the validity of the approximate formula $K_s = \frac{1}{2}U^2(1 - C_{pb})$, provided that a correct value of the base pressure coefficient, C_{pb}, is used. The vorticity balance in the laminar wake reveals that 70% of the vorticity shed is found in the vortices. Finally, the verification of the criteria for the formation length and for the first appearance of the vortices reported herein at different Reynolds numbers and other cylindrical cross-sections remains an interesting subject for further research.

References

Allen, H. J. & Vincenti, W. G. 1944 Wall interference in a two-dimensional flow wind tunnel, with consideration of the effect of compressibility. NACA Report 782, Washington.

Anagnostopoulos, P. 1989 Numerical solution for laminar two-dimensional flow about a fixed and transversely oscillating cylinder in a uniform stream. *Journal of Computational Physics* **85,** 434–456.

Anagnostopoulos, P. & Bearman, P. W. 1992 Response characteristics of a vortex-excited cylinder at low Reynolds numbers. *Journal of Fluids and Structures* **6,** 39–50.

Anagnostopoulos, P. 1994 Numerical investigation of response and wake characteristics of a vortex-excited cylinder in a uniform stream. *Journal of Fluids and Structures* **8,** 367–390.

Bearman, P. W. 1965 Investigation of the flow behind a two-dimensional model with a blunt trailing edge and fitted with splitter plates. *Journal of Fluid Mechanics* **21,** 241–255.

Berger, E. 1964 The determination of the hydrodynamic parameters of a Kármán vortex street from hot wire measurements at low Reynolds numbers. *Zeitschrift für Flugwissenschaften* **12,** 41–59.

Berger, R. & Wille, R. 1972 Periodic flow phenomena. *Annual Review of Fluid Mechanics* **4,** 313–340.

Birkhoff, G. & Zarantonello, E. H. 1957 *Jets, Wakes and Cavities,* New York: Academic Press.

Bloor, M. S. 1964 The transition to turbulence in the wake of a circular cylinder. *Journal of Fluid Mechanics* **19,** 290–304.

Bloor, M. S. & Gerrard, J. H. 1966 Measurements on turbulent vortices in a cylinder wake. *Proceedings of the Royal Society of London* A **294,** 319–342.

Braza, M., Chassaing, P. & Ha Minh, H. 1986 Numerical study and physical analysis of the pressure and velocity fields in the near wake of a cylinder. *Journal of Fluid Mechanics* **165,** 79–130.

Chilukuri, R. 1987 Incompressible laminar flow past a transversely vibrating cylinder. *Trans. ASME Journal of Fluids Engineering* **109,** 166–171.

Eaton, B. E. 1987 Analysis of laminar vortex shedding behind a circular cylinder by computer-aided flow visualization. *Journal of Fluid Mechanics* **180,** 117–145.

Franke, R., Rodi, W. & Schoenung, B. 1990 Numerical calculation of laminar vortex-shedding flow past cylinders. *Journal of Wind Engineering and Industrial Aerodynamics* **35,** 237–257.

Freymuth, P., Finaish, F. & Bank, W. 1986 Visualization of the vortex street behind a circular cylinder at low Reynolds number. *Physics of Fluids* **29,** 1321–1323.

Gerrard, J. H. 1966 The mechanics of the formation region of vortices behind bluff bodies. *Journal of Fluid Mechanics* **25,** 401–413.

Gerrard, J. H. 1978 The wakes of cylindrical bluff bodies at low Reynolds number. *Philosophical Transactions of the Royal Society of London* A **288,** 1354, 351–382.

Green, R. B. 1989 Measurements of vorticity and vortex strength in the wake of a circular cylinder at low Reynolds number. Ph.D. thesis, University of Manchester, Manchester, U.K.

GREEN, R. B. & GERRARD, J. H. 1991 An optical interferometric study of the wake of a bluff body. *Journal of Fluid Mechanics* **226,** 219–242.

GREEN, R. B. & GERRARD, J. H. 1993 Vorticity measurements in the near wake of a circular cylinder at low Reynolds numbers. *Journal of Fluid Mechanics* **246,** 675–691.

GRESHO, P. M., LEE, R. L. & SANI, R. L. 1980 On the time-dependent solution of the incompressible Navier-Stokes equations in two and three dimensions. In *Recent Advances in Numerical Methods in Fluids,* (eds C. Taylor & K. Morgan), pp. 27–79. Swansea: Pineridge.

GRIFFIN, O. M. & RAMBERG, S. E. 1974 The vortex-street wakes of vibrating cylinders. *Journal of Fluid Mechanics* **66,** 553–576.

HOOKER, S. G. 1936 On the action of viscosity in increasing the spacing ratio of a vortex street. *Proceedings of the Royal Society of London* A **154,** 67–89.

JORDAN, S. K. & FROMM, J. E. 1972 Oscillatory drag, lift, and torque on a circular cylinder in a uniform flow. *Physics of Fluids* **15,** 371–376.

KARNIADAKIS, G. E. & TRIANTAFYLLOU, G. S. 1989 Frequency selection and asymptotic states in laminar wakes. *Journal of Fluid Mechanics* **199,** 441–469.

KARMAN, T. VON 1991 Über den Mechanismus des Widerstandes, den ein bewegter Körper in einer Flüssigkeiterfährt. *Göttinger Nachrichten, mathematik-physik* Kl. 547.

KOOPMANN, G. H. 1967 The vortex wakes of vibrating cylinders at low Reynolds numbers. *Journal of Fluid Mechanics* **28,** 501–512.

NISHIOKA, M. & SATO, H. 1978 Mechanism of determination of the shedding frequency of vortices behind a cylinder at low Reynolds numbers. *Journal of Fluid Mechanics* **88,** 49–60.

OKUDE, M. & MATSUI, T. 1990 Vorticity distribution of vortex street in the wake of a circular cylinder. *Transactions of Japan Society of Aeronautics and Space Science* **33,** 1–13.

PERRY, A. E., CHONG, M. S. & LIM, T. T. 1982 The vortex-shedding process behind two-dimensional bluff bodies. *Journal of Fluid Mechanics* **116,** 77–90.

ROSHKO, A. 1954 On the development of turbulent wakes from vortex streets. NACA Report 1191, pp. 801–825.

ROSHKO, A. 1961 Experiments on the flow past a circular cylinder at very high Reynolds number. *Journal of Fluid Mechanics* **10,** 345–356.

SCHAEFER, J. W. & ESKINAZI, S. 1959 An analysis of the vortex street generated in a viscous fluid. *Journal of Fluid Mechanics* **6,** 241–260.

SMITH, S. L. & BREBBIA, C. A. 1977 Improved stability techniques for the solution of Navier-Stokes equations. *Applied Mathematical Modelling* **1,** 226–234.

STROUHAL, V. 1878 Über eine besondere Art der Tonerrenung. *Analen der Physik und Chemie* New Series **5,** 216–251.

SWANSON, J. C. & SPAULDING, M. L. 1978 Three dimensional numerical model of vortex shedding from a circular cylinder. In *Symposium on Non-Steady Fluid Dynamics,* pp. 207–216. New York: ASME.

TRITTON, D. J. 1959 Experiments on the flow past a circular cylinder at low Reynolds numbers. *Journal of Fluid Mechanics* **6,** 547–567.

VAN DYKE, M. 1982 *An Album of Fluid Motion.* Stanford: Parabolic.

WILLIAMSON, C. H. K. 1989 Oblique and parallel modes of vortex shedding in the wake of a circular cylinder at low Reynolds numbers. *Journal of Fluid Mechanics* **206,** 579–627.

WILLIAMSON, C. H. K. 1991 2-D and 3-D aspects of the wake of a cylinder, and their relation to wake computations. *Lectures in Applied Mathematics* **28,** 719–751.

ZDRAVKOVICH, M. M. 1969 Smoke observations of the formation of a Kármán vortex street. *Journal of Fluid Mechanics* **37,** 491–496.